Department of Physics and Astronomy

University of Heidelberg

Master thesis

in Physics

submitted by

Tim Sailer

born in Villingen-Schwenningen

2017

A Laser Ion Source for the ALPHATRAP Experiment

This Master thesis has been carried out by Tim Sailer

at the

Max-Planck-Institut für Kernphysik in Heidelberg

under the supervision of

Prof. Dr. Klaus Blaum

Dr. Sven Sturm

Dr. Robert Wolf

Eine Laserionenquelle für das ALPHATRAP-Experiment:

Das Penningfallen-Experiment ALPHATRAP, in dem vor kurzem erste Signale von einzelnen, in der Falle produzierten Ionen gemessen wurden, befindet sich am Max-Planck-Institut für Kernphysik in Heidelberg. ALPHATRAP ist das Nachfolge-Experiment des Mainzer g-Faktor Experiments und soll den g-Faktor des gebundenen Elektrons in schweren Ionen bis zu wasserstoffähnlichem $^{208}Pb^{81+}$ bestimmen. Diese Ionen werden extern produziert und durch eine Ultrahochvakuum-Ionentransportstrecke in die Falle injiziert. Um die Präzision der zukünftigen Messungen zu steigern, soll der Aufbau durch symphathetisches Laserkühlen mittels $^{9}Be^{+}$ Ionen erweitert werden. Durch das Kühlen in den niedrigen mK-Bereich wird die Ionentemperatur keine grundlegende Limitierung der momentanen Messgenauigkeit mehr darstellen und komplett neue Messmethoden werden ermöglicht. Das Erzeugen der Beryllium-Ionen erfordet eine eigene Ionenquelle. Hierfür wird eine Laserionenquelle (LIS), die im Rahmen dieser Arbeit entworfen, gebaut und getestet wurde, an die vorhandene Ionentransportstrecke angeschlossen. Es konnte gezeigt werden, dass die LIS eine erfolgreiche Produktion und Extraktion von etwa 3×10^{7} $^{9}Be^{+}$ Ionen pro Laserpuls erlaubt. Die Anzahl und Strahlqualität der produzierten Ionen erfüllen die Anforderungen des ALPHATRAP-Experiments.

A Laser Ion Source for the ALPHATRAP Experiment:

The Penning-trap experiment ALPHATRAP, where the first single in-trap produced ions could be observed recently, is located at the Max-Plack-Institut für Kernphysik in Heidelberg. ALPHATRAP is a follow-up to the Mainz g-factor experiment with the aim to measure the g-factor of the bound electron in heavy ions up to hydrogen-like $^{208}Pb^{81+}$. These ions are externally produced and will be injected into the trap via an ultra-high vacuum beamline. To increase the precision of the future measurements, sympathetic laser cooling via $^{9}Be^{+}$ ions is to be implemented into the setup. This will remove temperature as one of the main limitations of current measurement precision as well as allowing completely new measurement schemes by cooling to the few mK range. The production of beryllium ions requires a dedicated ion source. For this purpose, a laser ion source (LIS) was designed, built and tested in the context of this thesis and will be implemented in the existing beamline. The LIS has shown to successfully produce and allow an extraction of about 3×10^{7} $^{9}Be^{+}$ ions per laser pulse. The yield and the beam quality of the produced ions fulfills the required conditions of the ALPHATRAP experiment.

Contents

List of Figures

1 Motivation

A big part of modern physics is the strive to validate the predictions and applicability of theories about how the universe works. To do this, one can compare these theories to experimental results on ever increasing precision. For performing such experiments on charged particles with extremely high precision, Penning traps have been shown to meet the criteria that allow such measurements on single ions, protons or electrons. They have been used for example to measure the free electron g-factor [1], to determine the electron mass [2] with highest precision or to determine the g-factor of the bound electron in the hydrogen-like system $^{28}Si^{13+}$ [3], yielding the most stringent test of bound-state quantum electrodynamics (QED), one of the bases of the Standard Model of particle physics, yet.

Currently, the ALPHATRAP experiment is being set up at the Max-Planck-Institut für Kernphysik (MPIK) in Heidelberg, Germany, as a follow-up to the g-factor experiment in Mainz [2–5]. Its goal is to expand the measurements towards heavier systems up to hydrogen-like $^{208}Pb^{81+}$, where the last bound electron will be exposed to electric field strengths of up to $10^{18}\,\frac{\mathrm{V}}{\mathrm{m}}$, enabling tests of QED under extreme conditions. As ionization energies exceed $100\,\mathrm{keV}$ for such systems, an external ion source is required. The HD-EBIT [6], located at MPIK, will therefore be connected to the experiment via a beamline, allowing the injection of externally produced ions into the trap.

Among other things, it can be concluded from the measurements performed in Mainz that the ion temperature is still one of the limiting factors for the achievable precision, despite the whole setup already being operated at liquid helium temperature of about $4\,\mathrm{K}$. Therefore, it is necessary to further cool the ion in order to decrease systematic effects and make small effects easier to detect. Even though other methods such as electronic feedback cooling [7] have been applied to successfully cool the ion to $(1.7 \pm 1.0)\,\mathrm{K}$ [8], further cooling is still desirable. To achieve this, laser cooling is one of the best approaches and will be implemented in this experiment with the goal of gravely reducing the temperature down to a few mK. Since there are no suitable optical transitions available that can directly be utilized on highly charged ions, other ions will instead be cooled. By Coulomb interaction sympathetic cooling of the highly charged ion is possible. The ions used for this are $^{9}Be^{+}$ which can be cooled by a $313\,\mathrm{nm}$ laser that is currently being set up [9]. The production of these ions requires a dedicated ion source which will be a laser ion source (LIS) that will be coupled to the existing beamline, making use of the external transfer system into the trap. The design, production and testing of this LIS is discussed in this thesis.

The structure starts with a brief theoretical introduction into the concepts of QED and Penning traps, which are necessary to explain the ALPHATRAP setup and measurement

scheme. The total setup, including beamline for ion transport, vacuum systems and ion detection methods, such as micro-channel-plates (MCPs) and Faraday cups will then be outlined, also explaining time-of-flight (TOF) measurements. After that, the basics of Doppler laser cooling will be given and its application to highly charged ions will be discussed. Moving on to the main part, the design and production of the ion source will be covered. The LIS has proven to successfully produce the desired $^{9}Be^{+}$ ions in sufficient quantities which is shown and discussed in the measurements and results part. Finally, the thesis is concluded by giving an outlook of measurements and modifications yet to be done as well as the installation of the source at its designated position.

2 Theory

QED is a quantum field theory that expands electrodynamics to quantum level interactions as one of the foundations of the Standard Model of particle physics. It was developed by R. Feynman, J. Schwinger and S. Tomonaga [10] as a perturbation theory with virtual photons as intermediate particles. This was made possible by H. Bethe, who laid the foundation for renormalization calculations [11] to solve the problem of higher order terms diverging. With this, the theory was now able to explain the Lamb-Shift [12] observed in hydrogen, which can not be described using only Dirac theory. It corrects the calculation for charged particles in fields interacting with their own field and the vacuum, therefore slightly altering the Coulomb and magnetic interaction.

The precise calculations that QED allows for the free electron g-factor made it possible to test the theory with a relative uncertainty of 2.8×10^{-13} [1] when compared to the result of the $g/2$ measurement of the free electron g-factor. With the predictions made for bound systems, it was possible to achieve a relative uncertainty of 4×10^{-11} for the measurement of the g-factor in hydrogen-like $^{28}Si^{13+}$ performed in Mainz [3]. This is the most stringent test of bound-state QED in strong fields. Combined with the measurement of the lithium-like system $^{28}Si^{11+}$ with a relative precision of 1.1×10^{-9} [5] for many-electron systems, QED is the most precisely tested theory in physics. As QED describes interactions with electric fields and has for single ions in Penning traps only been tested precisely in the medium Z regime, ALPHATRAP aims to expand these measurements to even heavier systems, where the accessible field strength increases dramatically. In the case of hydrogen-like lead it possible to reach up to $10^{18}\,\frac{\mathrm{V}}{\mathrm{m}}$ for the electron in the electric field of the nucleus. This is especially interesting since most effects of interest exhibit a scaling with the nuclear charge or the corresponding electric field strength when looking at few to single electron systems.

In the following, an introduction to the values of interest is given, starting with the g-factor, explaining the experimental setup and measurement scheme and finishing with experimental limitations.

2.1 The free electron g-factor

Looking at the free electron as a charged particle with charge q, the total non-zero angular momentum $\vec{J}$ and its mass m_e, the magnetic moment μ_J is given as

$$\vec{\mu_j} = g_j \frac{q}{2m_e} \vec{J} \quad . \tag{2.1}$$

The dimensionless factor g_j is called the Landé g-factor with $\vec{\mu_j}$ being the total magnetic

moment resulting from both, Spin $\vec{S}$ and angular momentum $\vec{L}$. For the free electron there is no orbital angular momentum. Thus, $\vec{L}$ = 0 and equation (2.1) can be rewritten with the Bohr magneton $\mu_\mathrm{B} = {e\hbar}/{2m_\mathrm{e}}$, the reduced Planck constant $\hbar = {h}/{2\pi}$ and $q = -e$ the elementary charge, as

$$\vec{\mu_s} = -g_s \frac{e}{2m_\mathrm{e}} \vec{S} = -g_s \frac{\mu_\mathrm{B}}{\hbar} \vec{S} \quad . \tag{2.2}$$

The factor g_s is called the electron spin g-factor. First experimentally observed in the Stern-Gerlach-experiment in 1922 [13], this effect could only be described years later by the Dirac Theory which consistently combined special relativity with quantum mechanics for all massive particles with spin ${1}/{2}$ [14], and which results in g_s being exactly 2.

Taking QED into account, this value is shifted by additional correction terms, such as in first order the self energy, where the electron interacts with its own field. This results in a shift of $g = 2(1 + {\alpha}/{2\pi})$ [15], where α is the dimensionless fine-structure constant.

2.2 The g-factor of the bound electron

While the above holds true for a free electron, the additional effect of the field of the charged nucleus as well as a possible orbital angular momentum has to be considered in case of the bound electron. This relativistic contribution, when derived by solving the Dirac equation for an infinite mass nucleus and a point charge Z, is called the Breit Term [16]. For an hydrogen-like ion with the electron in the ground state it is given as

$$g_b = \frac{2}{3}\left(1 + 2\sqrt{1 - (Z\alpha)^2}\right) \quad . \tag{2.3}$$

The scaling of the dependance of this allows in principle the extraction of the fine-structure constant α. As it scales with the nuclear charge, measuring highly charged ions seems favorable if the experimental uncertainty of the measurement can be kept constant. It has to be considered though, that the theoretical uncertainty of the g-factor strongly increases with Z as well, limiting the achievable precision of the fine-structure determination. This is due to uncalculated higher order two-loop QED corrections and nuclear effects that greatly increase with Z [17]. The general scaling of the contributions to the g-factor of hydrogen-like ions is illustrated in figure 1.

A proposal by Shabaev might allow to counteract this increasing uncertainty by measuring a specific combination of the g-factors of boron- and hydrogen-like ions of the same spinless isotope in the lead region [17] due to many terms canceling out. A measurement following that scheme might allow a very precise determination of α, giving ALPHATRAP its name. Additionally the g-factor determination of highly-charged

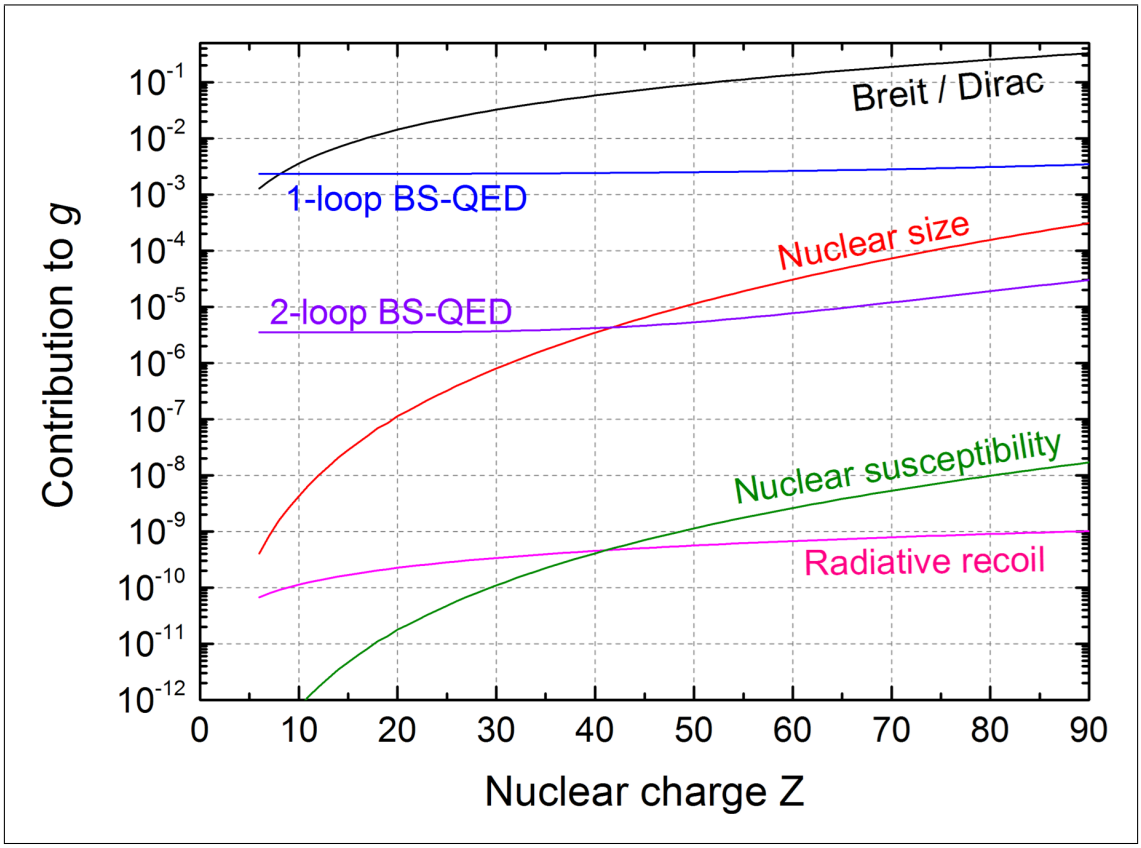

Figure 1: The scaling of different contributions to the g-factor of hydrogen-like ions with the nuclear charge [18].

ions allows a stringent test of the bound-state QED in very high field regimes, where higher order QED terms start to gain more significance, making such measurements very interesting.

The shown contributions as well as a possible angular momentum, when for example measuring a boron-like system, and vacuum polarization significantly alter this g-factor from the free electron g-factor. Since ALPHATRAP will measure bound systems in the ground state, in the following the term g-factor is always referring to that.

2.3 The ALPHATRAP experiment

To perform measurements on highly charged ions ALPHATRAP will use a Penning trap where, a strong homogenous magnetic field is overlapped with a weak electrostatic quadrupole field [19]. Considering only the magnetic field $\vec{B}$ and the resulting Lorentz force $\vec{F_{\mathrm{L}}} = q \cdot \vec{v} \times \vec{B}$, an ion with charge q and mass m_{ion} will perform a circular motion with the so called cyclotron frequency ω_c

$$\omega_c = \frac{q}{m_{\mathrm{ion}}} \cdot B \quad , \tag{2.4}$$

confining the particle radially. The axial confinement is achieved by applying a electrostatic quadrupole field

$$\Phi(x, y, z) = \frac{V_0}{2d^2}\left(z^2 - \frac{1}{2}(x^2 + y^2)\right) \text{ with } d^2 = \frac{1}{2}\left(z_0^2 + \frac{r_0^2}{2}\right) \quad . \tag{2.5}$$

In this equation, V_0 is the potential difference between the end caps and ring electrode, d is called the characteristic trap size, r_0 is the smallest radius in the hyperbolic electrode design and $2z_0$ is the distance between the end caps [20], see figure 2 (a). The cylindrical design of a Penning trap, as used in the ALPHATRAP experiment, is illustrated in figure 2 (b). The shape is easier to manufacture and allows for easy direct axial access.

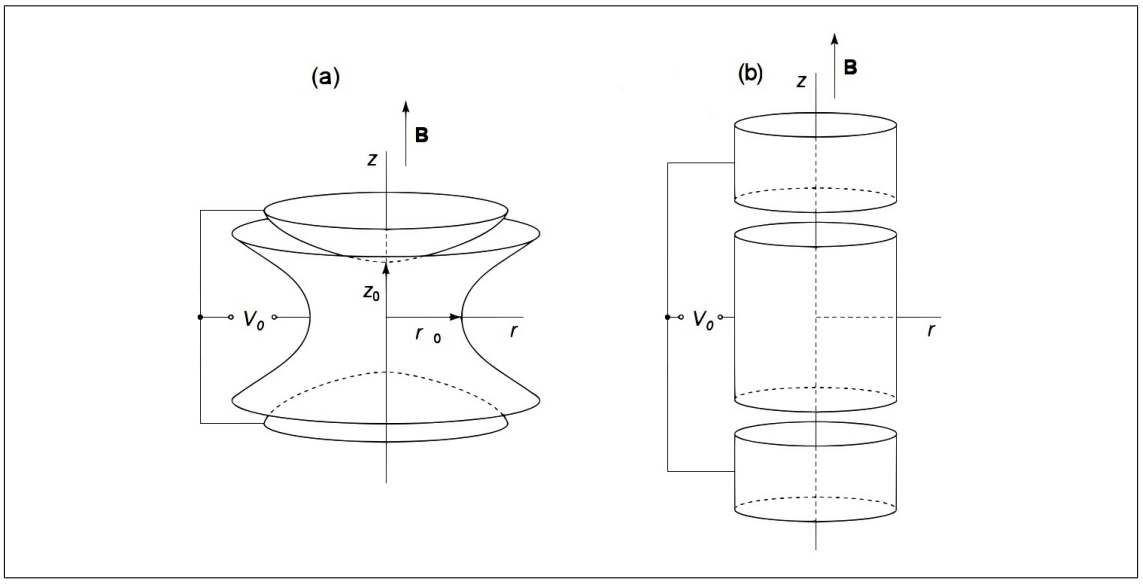

Figure 2: Depiction (a) shows an hyperbolical electrode design, (b) the cylindrical design with both consisting of a center ring electrode and two end caps [21].

Solving the equation of motion for the ideal quadrupole field yields three independent harmonic oscillations with the eigenfrequencies ω_z for the axial motion in z-direction,

ω_+ which is called the modified cyclotron frequency and ω_- the magnetron frequency, both describing a motion around the trap center [19] as illustrated in figure 3.

$$\omega_z = \sqrt{\frac{qV_0}{m_{\text{ion}}d^2}} \tag{2.6}$$

$$\omega_+ = \frac{\omega_c}{2} + \sqrt{\frac{\omega_c^2}{4} - \frac{\omega_z^2}{2}} \tag{2.7}$$

$$\omega_- = \frac{\omega_c}{2} - \sqrt{\frac{\omega_c^2}{4} - \frac{\omega_z^2}{2}} \tag{2.8}$$

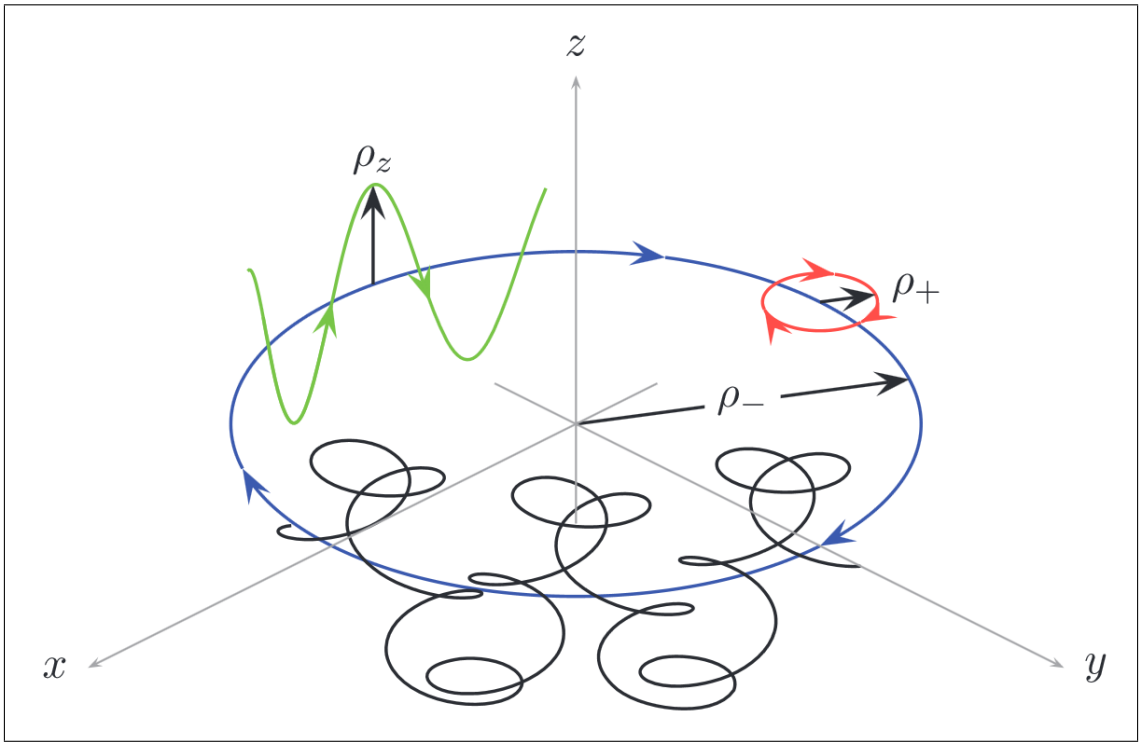

Figure 3: An exemplary ion motion (black) shown as a combination of magnetron motion ρ_- (blue), modified cyclotron motion ρ_+ (red) and axial motion ρ_z (green). Adapted from [22].

The splitting of the radial motion into two separate motions is due to the quadrupole potential in radial direction, resulting in a position dependent total force when combined with the constant Lorentz force. From equation (2.7) and (2.8) the stability criteria can directly be obtained:

$$\omega_c^2 \geq 2\omega_z^2 \quad . \tag{2.9}$$

Combined with equation (2.4) and (2.6) it becomes

$$V_0 \leq \frac{qd^2}{2m_{\text{ion}}} \cdot B^2 \quad , \tag{2.10}$$

which shows why the magnetic field is chosen to be quite strong since it directly limits the allowed electric potential.

Furthermore, the invariance theorem by Brown and Gabrielse [19] gives the following relation between the three independent eigenfrequencies (2.6) - (2.8), which gives access to the actual free cyclotron frequency ω_c:

$$\boxed{\omega_c^2 = \omega_+^2 + \omega_-^2 + \omega_z^2} \quad . \tag{2.11}$$

This makes the free cyclotron frequency invariant to imperfections such as alignment errors of the trap in the magnetic field or an ellipticity in the harmonic potentials. The measurement of the three eigenfrequencies is achieved by measuring the image current in the trap electrodes induced by the oscillating ion [23, 24]. To do this, tuned circuits are operated at liquid helium temperatures to reduce thermal noise to a minimum. Due to the continuously induced current in the attached circuits by the ion, energy gets transferred to the helium bath thus cooling the ion as a result until a thermal equilibrium is reached. Temperatures close to the liquid helium temperatures have been observed, reaching for example $T_z = (4.8 \pm 0.3)\,\text{K}$ [5] – which is in good agreement with the estimated lattice temperature of $(4.2 \pm 1.0)\,\text{K}$ [23] which would be reached, if no additional heating or noise was existent. With an additional feedback cooling, temperatures as low as $(1.7 \pm 1.0)\,\text{K}$ have been observed [8].

2.3.1 g-factor measurement in Penning traps

Since the ion is stored in a magnetic field, the magnetic moment caused by the electron will align either parallel or anti-parallel to the magnetic field. These two different possibilities result in an energy splitting, known as the Zeeman-effect, giving the following two states:

$$E_\pm = E_0 + \vec{\mu_s} \cdot \vec{B} = E_0 \pm g_s \frac{\mu_\text{B}}{2} B \quad . \tag{2.12}$$

Consequently, the energy difference between those two states is

$$\Delta E = \hbar \omega_L = g_s \mu_\text{B} B \tag{2.13}$$

with the frequency ω_{L} being the Larmor frequency. By combining equation (2.13) with (2.4) this becomes

$$\boxed{g_s = 2 \cdot \frac{\omega_{\mathrm{L}}}{\omega_{\mathrm{c}}} \cdot \frac{q_{\mathrm{ion}}}{e} \cdot \frac{m_e}{m_{\mathrm{ion}}}} \quad , \tag{2.14}$$

showing that the $\vec{B}$ field has not to be measured separately but drops out of the final equation. This reduces the quantities to be measured to the free cyclotron frequency ω_c and the Larmor frequency ω_{L}, assuming that the masses of the ion m_{ion} as well as the mass of the electron m_{e} can be obtained by independent experiments. If QED calculations for the g-factor are assumed to be correct instead of testing them, this equation can be solved for m_{e}, giving direct access to the mass of the electron [2].

2.3.2 The continuous Stern-Gerlach effect

Since the spin of the electron and thus the Larmor frequency are not coupled to the motion of the ion in a perfectly homogenous field other than through small relativistic effects, the Larmor frequency cannot be measured directly. It is possible, however, to achieve such a coupling of the spin state to the ion frequency by modifying the magnetic field. If the energy difference between those spin states can be measured, the Larmor frequency can be determined.

As a magnetic field will never be perfectly homogenous but always consist of higher order terms, it can be expressed by expanding the field in z-direction in Legendre polynomials

$$B_z = B_0 - 2B_1 z + B_2 \left(z^2 - \frac{1}{2}\rho^2 \right) + \ldots \quad . \tag{2.15}$$

B_0 is the main magnetic homogenous field part, B_1 is a linear dependence of the field along the z-axis and the B_2 term can be described as a magnetic bottle. The magnetic moment of the ion stems from the combination of the electron magnetic moment $\mu_{\mathrm{z,spin}}$ and the ion motion. For the ion motion, only the reduced cyclotron motion is considered since the magnetron contribution is significantly smaller and can be neglected [23]. This results in a total magnetic moment of

$$\mu_z^{\pm} = \mu_z^{\mathrm{cycl}} + \mu_z^{\mathrm{spin}} = -\frac{q_{\mathrm{ion}} E_+}{m_{\mathrm{ion}} \omega_+} \pm \frac{g_s \mu_{\mathrm{B}}}{2} \quad . \tag{2.16}$$

This magnetic moment causes the additional magnetic potential

$$\Phi_{\mathrm{mag}} = \left(-\frac{q_{\mathrm{ion}} E_+}{m_{\mathrm{ion}} \omega_+} \pm \frac{g_s \mu_{\mathrm{B}}}{2} \right) B_z \tag{2.17}$$

which, if neglecting the small linear term of B_z, can be written as

$$\Phi_{\text{mag}} = \mu_z^{\pm} \left(B_0 + B_2 \left(z^2 - \frac{1}{2}\rho^2 \right) \right) \tag{2.18}$$

which causes an cyclotron energy E_+ and spin orientation dependent potential difference. This shift in the magnetic potential in z-direction is therefore directly linked to the orientation of the spin of the electron and the ions cyclotron energy, which alters the initial axial frequency $\omega_{z,0}$ to

$$\omega_z^{\pm} = \sqrt{\omega_{z,0}^2 - \frac{2\mu_z^{\pm} B_2}{m_{\text{ion}}}} \tag{2.19}$$

$$\approx \omega_{z,0} - \frac{\mu_z^{\pm} B_2}{m_{\text{ion}} \omega_{z,0}} \tag{2.20}$$

$$= \omega_{z,0} + \left(\frac{q_{\text{ion}} E_+}{m_{\text{ion}} \omega_+} \mp \frac{g_s \mu_{\text{B}}}{2} \right) \frac{B_2}{m_{\text{ion}} \omega_{z,0}} \tag{2.21}$$

and thus

$$\Delta\omega_z \approx \frac{g_s \mu_{\text{B}} B_2}{m_{\text{ion}} \omega_{z,0}} \quad . \tag{2.22}$$

This effect, called the continuous Stern-Gerlach effect, was first proposed by Dehmelt [25] to be utilized for the non-destructive spin state detection if the electron, or ion in this case, is stored in a Penning trap. The dependence of the shift is therefore proportional to the B_2 coefficient, making a large value desirable especially since the shift becomes smaller for higher ion masses. This can be achieved by using a ring electrode made of ferromagnetic material resulting in a magnetic bottle. Furthermore, since the frequency will also shift with changes of the cyclotron energy E_+, a very small and stable temperature is required.

The ions energy E_+ can be written as

$$E_+ = \frac{1}{2} m_{\text{ion}} \omega_+^2 r_+^2 \quad . \tag{2.23}$$

Since the ion cyclotron motion is not coupled to a resonator, it is in principle fixed in energy. However, patch-potentials and electronic noise, which can reasonably be approximated white noise in the range of the ions frequency will cause a resonant excitation of the ions motion. This results in the energy E_+ performing a random walk depending on the present noise. As the resonant excitation results in a constant change of the ions radius Δr_+, a larger radius directly corresponds to a larger shift of E_+ since it is proportional to the current radius squared. This means that the fluctuation of the axial frequency $w_{z,0}$ is increasing with the ions radius as can be seen in equation

(2.21). Therefore, a reduction of the cyclotron energy of the ion directly results in an increased stability of the axial frequency. This has to be sufficiently stable to differentiate between spin-flips and random temperature fluctuations. If the energy is assumed to follow $E_+ = k_B T$, a change of approximately $\Delta T_+ \approx 5.6\,\mathrm{K}$ produces the same shift as a spin-flip would. A temperature stability significantly below this is therefore required to unambiguously detect a spin-flip. This is one of the reasons why laser cooling is an interesting prospect for this experiment.

The general idea of the magnetic bottle and the design of the trap used in ALPHATRAP are illustrated in figure 4.

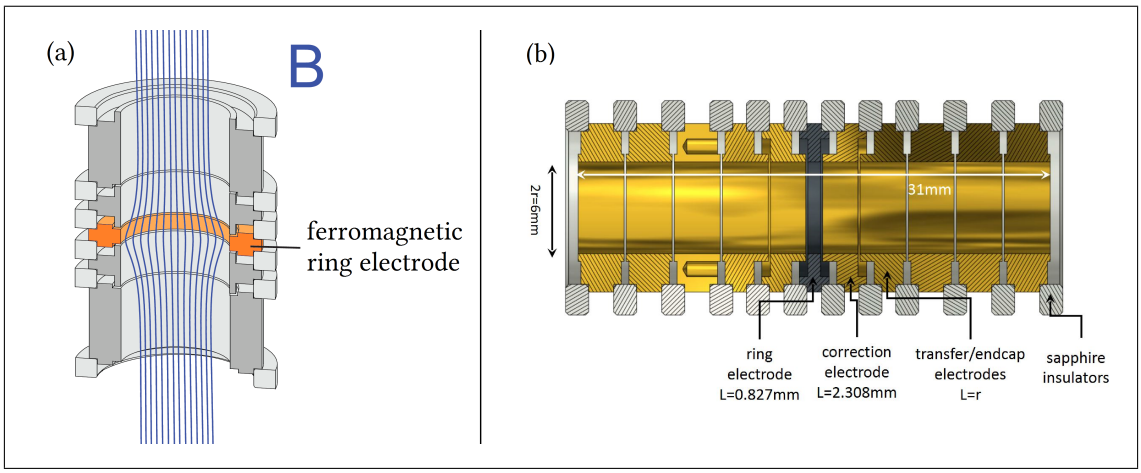

Figure 4: On the left side (a) the principle of the ferromagnetic ring causing a high B_2 is illustrated [24], picture (b) shows the actual design of the trap used for the spin state detection in the ALPHATRAP experiment with the gray center electrode being the ferromagnetic ring electrode.

This design can achieve B_2 values of $B_2 \approx 4.5 \times 10^4\,\frac{\mathrm{T}}{\mathrm{m}^2}$ while the axial frequency is $\nu_z \approx 300\,\mathrm{kHz}$. For the example of $^{208}\mathrm{Pb}^{81+}$ this would make the frequency shift to be $\Delta\nu_z \approx 200\,\mathrm{mHz}$.

2.3.3 The Larmor frequency and double Penning trap

The inhomogeneity achieved through the modification disscussed in section (2.3.2) is necessary to detect the spin state but causes problems when measuring the eigenfrequencies of the ion. Due to the B_2 coefficient, systematic shifts of the eigenfrequencies of the ion occur and would result in very low precision measurements. The solution to this problem is to use two separate traps instead of the same for both measurements. One of them – the precision trap (PT) – has a very homogenous field (e.g. $B_2 \approx 0$) and will be used to measure the eigenfrequencies, whereas the other trap – the analysis trap (AT) as

shown in figure 4 – has a very strong B_2 coefficient caused by a ferromagnetic ring for the spin state detection. This setup is known as the double Penning-trap system and has successfully been used for many measurements connected to g-factors [4, 5, 21, 26]. The design of the complete ALPHATRAP Penning-trap setup is illustrated in figure 5.

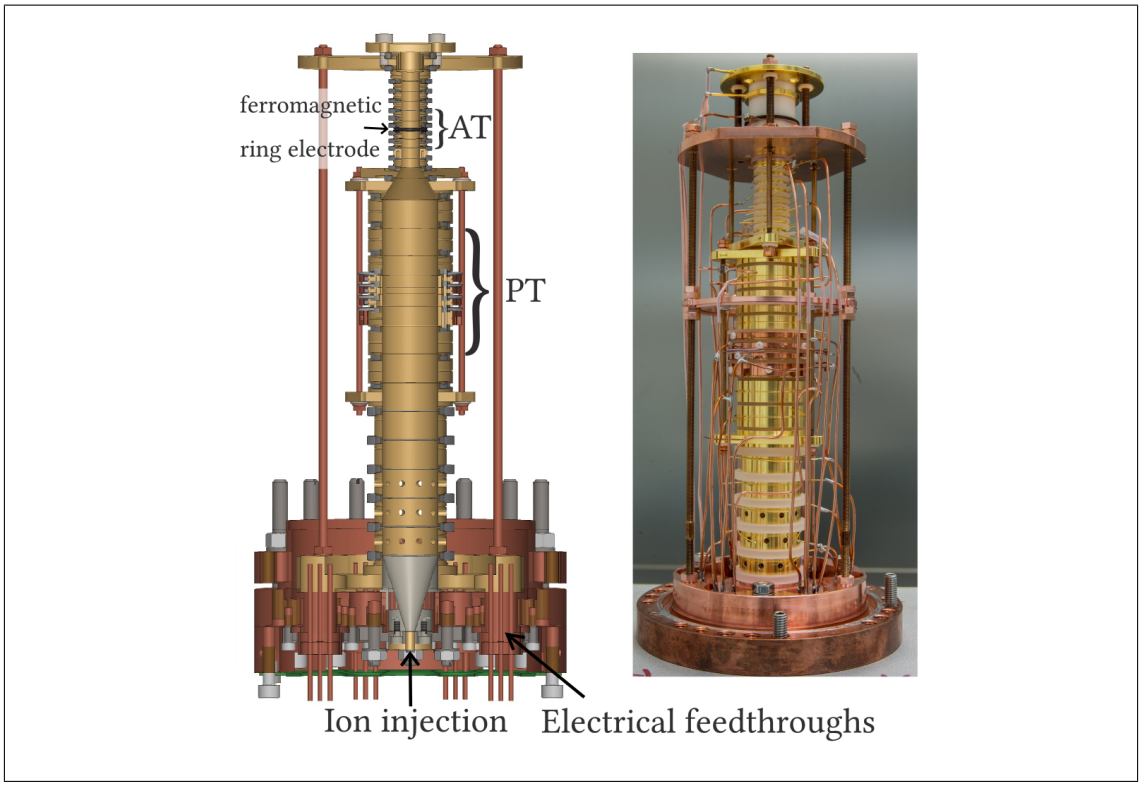

Figure 5: Complete design of the trap of the ALPHATRAP experiment. The left side shows the CAD model with a cut along the z-axis, on the right side the fully assembled trap is shown. The trap consists of the combination of the AT and PT as labeled, the additional electrodes are used for ion transportation. The difference of size between AT with the electrode radius of $r = 3\,\mathrm{mm}$ and PT with $r = 9\,\mathrm{mm}$ is required to keep a strong B_2 in the AT (small diameter) but to minimize the image charge shift of the cyclotron frequency in the PT that scales with the ion mass $\propto m_{\mathrm{ion}}$ and with the inverse cubic trap electrode radius $\propto 1/r^3$. The trap tower is rotated by $180°$ in the setup to inject the ions from the top.

With the spin state now detectable in the AT, the energy difference between the two states has to be determined to extract the Larmor frequency. To do this, a spin flip has to be induced. This can be achieved by irradiating a microwave into the trap via a dedicated antenna. If the frequency of the irradiated wave matches the Larmor frequency and is absorbed, a spin flip will be observed. However, this spin flip needs to be done while the ion is in the PT, where the measurement of the eigenfrequencies is performed in a different magnetic field compared to the AT.

To make the measurement possible despite that, the ion has to be prepared in a well defined spin state in the AT. Inducing a spin flip there, will either shift the frequency up or down determining the current associated spin state. With this known, the ion is adiabatically transferred to the PT.

Now the motional eigenfrequencies will be measured, while a frequency close to the expected Larmor frequency is irradiated again. After transferring back into the AT, the spin state can be checked by inducing yet another spin flip. If the spin was initially prepared in the state corresponding to a higher frequency and was changed in the PT, it will again increase when checking in the AT thus a spin flip in the PT can be concluded – and vice versa for the lower frequency starting state.

This measurement is performed with different irradiated frequencies each cycle, while monitoring the spin flip probability. This probability of observing a spin flip will show a maximum for the frequency exactly matching the Larmor frequency. An exemplary measurement of this process is shown in figure 6, with Γ being the ratio of Larmor frequency to free cyclotron frequency $\Gamma = \omega_L/\omega_c$.

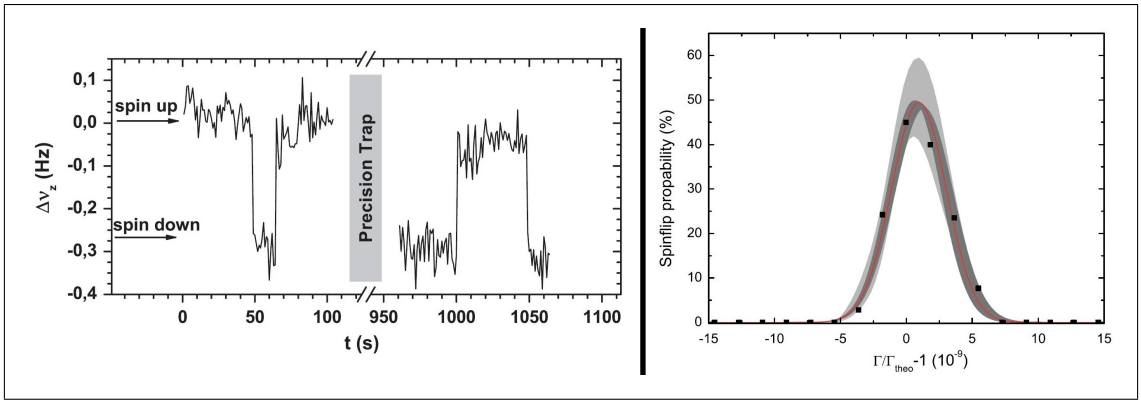

Figure 6: The left picture shows the successful measurement scheme with a spin flip happening in the AT performed in Mainz for a $^{28}Si^{13+}$ ion. It was transported to the PT with the frequency being in the higher mode and when it came back the next measured spin flip again caused it to jump from the lower to the higher mode. The right side shows the plot with the fitted probability to induce a spin flip for several hundred measurements. The shift compared to the theoretical value Γ_{theo} is due to the measured values not being corrected for systematic shifts yet [3].

2.4 Field inhomogeneities and frequency shifts

Field inhomogeneities can induce frequency shifts, such as the one used in the continuous Stern-Gerlach effect. Unwanted possible effects of considerable size are among others the following:

2.4.1 Effects of magnetic inhomogeneity

Ideally, a perfectly homogenous magnetic field in the PT and a strong B_2 coefficient of the magnetic field in the AT are desirable. This is not perfectly possible because, firstly, the tail of the magnetic bottle caused by the ferromagnetic ring in the AT will still be visible in the PT. For the ALPHATRAP setup, a compensation ring is used that corrects for the biggest part of the B_2 introduced in the AT. Secondly, the magnet will contribute a B_2 part which, despite coils to minimize this effect, causes the main magnetic inhomogeneity in the PT. While the shift depending on the electron spin orientation in the axial frequency in the AT is necessary, it is causing problems in the PT by allowing a coupling of the former independent frequencies, thus changing them slightly. The axial frequency, for example, scales with

$$\frac{\Delta\omega_z}{\omega_z} = \frac{B_2}{4B_0}\frac{\omega_+ + \omega_-}{\omega_+\omega_-}\left(\hat{\rho}_-^2\omega_- + \hat{\rho}_+^2\omega_+\right) \quad , \tag{2.24}$$

with $\hat{\rho}$ being the ion motional radius in cylindrical coordinates of the respective motion [27].

2.4.2 Electric field

As one can easily see from the effect of the magnetic bottle and the resulting B_2 coefficient, inhomogeneities result in the frequencies no longer being independent. This is not only true for magnetic inhomogeneities but also for electric field anharmonicities. The Legendre expansion of the electric field, as done for the magnetic field, can be written as [27]

$$\Phi(r,\Theta) = \sum_k C_k r^k P_k(\cos\Theta) \quad . \tag{2.25}$$

The odd terms will cancel out due to the cylindrical symmetry of the trap, but the even terms, foremost the anharmonic C_4 contribution, cause an ion radius frequency dependence [28] with

$$C_4 = C_4^0 + D_4\frac{U_c}{U_0} \quad , \tag{2.26}$$

where U_c is the applied correction electrode voltage, U_0 is the end cap voltage and D_4 is given by the trap geometry. In the case of the ALPHATRAP experiment with a compensated seven electrode trap, the C_4 and C_6 terms can be set to zero by applying the correct voltages. The compensation of the trap, a geometrical feature of the electrode shape, provides that even C_8 and C_{10} are as close to zero as the machining precision allows. Here, only a detuning of the correction voltage is considered that causes a residual C_4,

resulting in a scaling of the axial frequency [27] as

$$\frac{\Delta\omega_z}{\omega_z} = \frac{C_4}{C_2}\frac{3}{4d^2}\left(\hat{\rho}_-^2\omega_- + \hat{\rho}_+^2\omega_+\right) \quad . \tag{2.27}$$

2.4.3 Relativistic effects

The relativistic shifts are directly connected to the ion energy for the different modes. Due to mass changes corresponding to the kinetic energy of the ion, the frequencies are directly affected. This exhibits a scaling with $\propto E/mc^2$ for all frequencies, where E is the corresponding energy of the motion.

2.4.4 Scaling of field effects

The correction calculations have been rigorously performed by Ketter *et al.* [27] giving the precise dependance of the scaling of all frequencies up to B_4 or C_8 contributions. From this, the dependence on the field coefficients as well as the relativistic motion can be understood. Especially noteworthy is the scaling of all, magnetic, electric and relativistic shifts with the energies of the individual motions which corresponds to their radius. This dependence demonstrates again, why lower temperatures are of advantage, keeping the shifts small and explaining the interest in laser cooling.

Since the measurement of the eigenfrequencies by the image current technique depends on the induced current by the motion of the ion, the detection becomes more complicated when the motion becomes smaller. To be able to take advantage of the reduced frequency shifts at lower temperatures, a measurement technique applicable at such temperatures is required. The PnA (Pulse 'n' Amplify) technique [23] makes this possible and removes such measurement restrictions. With this phase sensitive measurement procedure, it is of advantage to cool the cyclotron mode to temperatures as low as possible, leaving the image charge shift [23] as largest restriction on the achievable precision of the measurement.

2.5 The PnA measurement technique

PnA provides a means of a phase-sensitive measurement of the ion's cyclotron frequency. The measurement scheme starts by preparing the ion's cyclotron motion with a well defined initial phase and amplitude by applying an excitation pulse. The cyclotron motion is then allowed to evolve freely for a certain time. Now, a quadrupole pulse is used to transfer the phase information of the cyclotron mode to the axial mode to enable a measurement of the evolved phase [23, 26, 29].

The precision of the initial phase definition with the excitation pulse and the read-out precision determine the achievable frequency resolution. The thermal distribution of the cyclotron radii of the ion is a dominant source of uncertainty for this. To achieve a sufficient phase resolution, the excitation amplitude needs to be high enough to overcome this uncertainty. Therefore, higher starting temperatures of the ion require a larger ion amplitude. This decreases the overall precision though, as the systematic shifts will increase. For this type of measurement, a temperature as low as possible is therefore desirable. As laser cooling offers the possibility to cool the ion below otherwise achievable temperatures, it is of great interest for measurements performed with PnA.

2.6 Doppler Laser cooling and application for ALPHATRAP

The basic principle of laser cooling requires a bound electron to be excited to a fast decaying state by the absorption of a photon. To this end, the transition energy between the initial and the excited state of the electron has to match the photon energy. Due to the momentum of the photon, that is transferred to the ion when absorbed, the momentum of the ion is changed. If this can be done contentiously to effectively lower the momentum, a cooling can be achieved.

Since the required excitation energy of an electron increases with the charge state of the ion, the energy exceeds easily accessible transitions for HCIs. The few transitions left, for which lasers with suitable wavelengths do exist, can in general not be used for laser cooling since the transitions are forbidden and therefore to slow to be used for an effective cooling. Additionally, even if it could be done, this would highly restrict the possible species that can be measured, while also requiring a different wavelength for each species – which usually means a different laser system.

The solution to this problem is sympathetic cooling. For this, another ion is laser cooled and coupled to the HCI of interest via Coulomb interaction. The ion to be cooled here is $^9Be^+$ as it has been successfully used for sympathetic cooling in Penning traps by Wineland *et al.* [30]. Additionally, as the trap is used for ions close to a charge-to-mass ratio $q/m \approx 1/2$, it is desirable to have the cooled ion as close as possible to the same ratio. Because the cooled ion has to be lowly charged, the lightest ion with a suitable transition is chosen, which is $^9Be^+$. Since this can be used to cool any other ion, the cooling process becomes independent of the species to be measured, making the setup very versatile.

2.6.1 Basic principle of Doppler laser cooling

The $2s^2S_{1/2}$ to $2p^2P_{3/2}$ transition in $^9Be^+$ allows for the resonant excitation of the electron with a wavelength of about $313\,\mathrm{nm}$. If the photon energy exactly matches the required

transition energy of the electron, the probability of the photon to be absorbed is highest. The momentum $p = {}^{h}/_{\lambda}$ of the absorbed photon is then transferred to the ion. Because the lifetime of the excited state is only in the ns range, the fast decay happens mostly due to spontaneous emission. In this case, the direction of the emitted photon is completely random, resulting in a change of momentum of the ion over several such cycles, where the absorption direction is determined by the laser beam direction while the emission direction is random.

To use this process for cooling, the laser is slightly detuned towards lower frequencies or so-called *red detuned*. When the ion now moves towards the laser, it sees a slightly shifted frequency due to the optical Doppler effect. The probability of an absorption is again highest, if this shift matches the detuning of the laser.

Due to the spontaneous emission afterwards, there is a net loss of total momentum of the ion in the direction towards the laser beam, effectively cooling that motion. The final temperature achievable by pure Doppler cooling is limited by the finite natural linewidth Γ of the transition which broadens the range of photons absorbed. This makes the cooling inefficient, if the optical Doppler shift gets close to the natural linewidth. It is given as

$$T_D = \frac{\hbar\Gamma}{2k_B} \quad , \tag{2.28}$$

with k_B being the Boltzmann constant. This limit is the steady state where heating and cooling are in equilibrium and is in the range of $500\,\mu\mathrm{K}$ for cooling $^9\mathrm{Be}^+$ ions.The single photon recoil limit, based on the fact that the theoretical minimal momentum of the ion can be brought down to that of the last emitted photon, is always below the limit of the transition linewidth [31, 32]. This limit is in the range of $500\,\mu\mathrm{K}$ for cooling of $^9\mathrm{Be}^+$ ions.

2.6.2 Application in ALPHATRAP

In most applications laser cooling is used for all directions, requiring three lasers to be overlapped from x, y and z direction. To improve the cooling time and hold the cooled particle in place, this can even be expanded to have the beams coming from both directions on each axis, requiring six laser beams for example in an optical molasses [33].

Due to the nature of ALPHATRAP being a Penning-trap experiment, there are special limitations. The radial access is not easily possible due to the design of the superconducting magnet with an axial bore. For this, the beamline (see figure 7) to transfer the ions into the trap as well as the microwave antenna needed for Larmor frequency measurements restrict the available space severely. Due to the ion already being stored and being well controlled, a cooling of all directions is not required though. This is because of

the possibility of the individual motions to be coupled to each other by modifications of the electric field. By applying radio frequency signals on the electrodes, the quadrupole field can be changed, resulting in a controlled coupling of the motions to each other [23]. When such a coupling is used, energy is transferred between the modes – which makes it possible to only use laser cooling on the axial mode while still being able to cool the radial modes as well.

This will be done as one directional cooling of the axial motion and is planned to be combined with the microwave access from below the magnet. Since this project, as addition to ALPHATRAP, is still in the process of being set up, it is very much prone to change and no specific parameters can be given yet. More details about this can be found in the thesis of Sandro Kraemer [9].

The required Coulomb interaction between the ions can be achieved in two possible ways. The first and most obvious is to simply store them together in the same trap. By being close together, they directly interact and while the beryllium ion is actively cooled, it cools the HCI as well. Since the eigenfrequencies would be shifted by this and thus can not be determined as precisely as required, they have to be measured before the cooling ion is brought into the trap.

When the ions are afterwards trapped together, cooling the beryllium ion towards the Doppler limit to achieve temperatures of both ions in the few mK range, results in the two ions forming a coulomb crystal due to their confinement in the trapping potential.

This theoretically opens the possibility to perform a "$g_1 - g_2$" measurement of the crystallized ions. As the achievable precision increases when the absolute difference between the g-factors becomes smaller, very precise measurements such as isotopic effects or differences between ions with similar masses can be performed.

With the magnetic field already being known to a 10^{-10} precision from the measurement of the eigenfrequencies beforehand, the achievable precision of the measured g-factor difference can be increased significantly. This would allow a stringent test of QED terms predicting that difference. A measurement following this scheme is planned to be used in the future of the ALPHATRAP experiment [34, 35].

The second option would be to have a cloud of some 10^6 beryllium ions stored in another section of the trap tower. They could be cooled there while the coupling could be achieved by electrically connecting the end caps (or any of the correction electrodes) of the HCI trap and the beryllium trap, achieving a coupling by the induced image charges. This is expected to enable cooling possibilities beyond the current temperature limitations.

To produce the $^9\mathrm{Be}^+$ ions required for laser cooling in the current setup, a dedicated laser ion source has been built in the context of this thesis. The general setup and integration into the ALPHATRAP setup will be covered in the next chapter.

3 Laser ion source

ALPHATRAP is connected to a beamline for the transport of externally produced ions into the trap. This beamline is operated at an ultra-high vacuum (UHV) down to $6 \times 10^{-11}\,\mathrm{mbar}$ requiring the ion source attached to it to be operable at a similar good vacuum. To be able to trap multiple externally produced ions, they have to arrive bunched to allow the in-trap lowering of their energy. Furthermore, the distance of about $4.5\,\mathrm{m}$ between the source and the trap makes an efficient ion transportation system necessary, which requires a well-defined ion beam. Specifically, that means it has to be minimized in space to pass through quadrupole benders and ion optics as well as temporally focused to make the selection of the species and trapping of the ions possible. An overview of the current beamline setup is shown in figure 7 and is discussed in more detail in the thesis of Henrik Hirzler [36] and Alexander Egl [37]. Additionally, since beryllium and its compounds are typically solid materials, it is convenient to vaporize it directly in the ion source minimizing safety hazards due to beryllium particles being toxic when inhaled. A laser ion source (LIS) is expected to fulfill these demands nicely.

3.1 Working principle of a laser ion source

The creation of ions from a solid material by a LIS can be achieved by two different techniques. For both, the material has to be ablated or vaporized first. This can be done by a high-intensity laser pulse heating up the material on a very short timescale, causing a fast vaporization. The material then explosively moves away from the target surface. To ionize the ablated atoms, photo-ionization can be utilized. For beryllium this would require a photon with $9.32\,\mathrm{eV}$, which corresponds to a wavelength of about $133\,\mathrm{nm}$, or high enough intensities enabling a two photon process starting at a wavelength of $266\,\mathrm{nm}$, respectively.

The second possibility is to use a laser pulse with a power density high enough to ignite a plasma in the ablated material. If the power is high enough to heat the material well above its boiling point, ions with energies up to several hundred eV are produced [38]. Even though the created plasma viewed as a whole is initially observed to be electrically neutral, ions can be extracted. This is explained in literature [39–41] by electrons moving faster than the nuclei because of their significantly lower mass while having the same thermal energy in the plasma. This makes the electrons more likely to hit the surrounding electrodes in the extraction region, leaving a net of positively charged ions. Similarly, a charge separation process can be assumed due to the higher velocities, causing a faster diffusion of electrons compared to the ions. Due to the applied electric field of some $10^5\,\frac{\mathrm{V}}{\mathrm{m}}$ those ions are accelerated out of this acceleration section of the LIS.

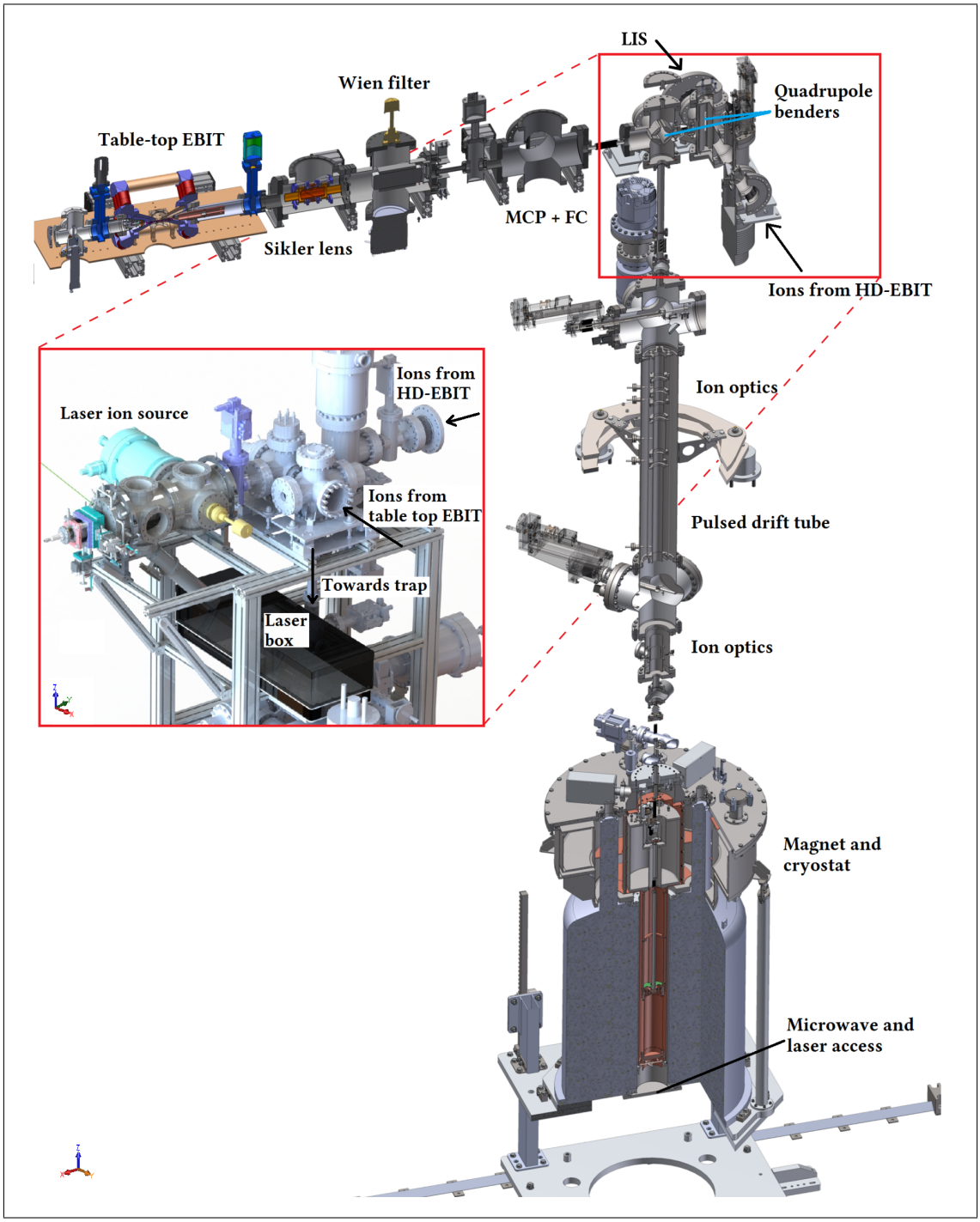

Figure 7: Overview of the ALPHATRAP experimental setup. Multiple ion sources are connected, starting from the table-top EBIT for lighter HCIs and later on the HD-EBIT for the heavy HCIs. The LIS will be attached to one of the two quadrupole benders, requiring the ion beam to pass through both benders and down towards the trap. The pulsed drift tube is used to decelerate the ion beam and then steer it into the trap with the last ion optics.

Another approach is to consider the thermally expanding plasma until the plasma density is low enough for the ions to be separated from the electrons by the applied voltages and allow an extraction [38, 42]. This is typically done with very high extraction voltages in the range of $50\,\mathrm{kV}$ [41] and will not be used for this setup.

Since this method of ionization doesn't require a specific wavelength, the laser can be chosen solely by its pulse power density $P_\mathrm{D} = {}^{E_\mathrm{p}}/_{t_\mathrm{p} A}$, defined as laser energy E_p per pulse duration t_p and beam spot area A. The power density required to ignite a plasma is slightly depending on the material but has been shown to be of the order of $P_D \approx 10^8\,\frac{\mathrm{W}}{\mathrm{cm}^2}$ [43–45]. By adjusting that to the target material a LIS can be used for the ionization of metals, such as aluminum, copper and beryllium but also for other materials such as carbon for the production of carbon cluster ions [45, 46].

For this setup a Nd:YAG laser (Litron Nano S) is used that provides $60\,\mathrm{mJ}$ per pulse at $1064\,\mathrm{nm}$ with a pulse length of $6–8\,\mathrm{ns}$ and a beam diameter of $4\,\mathrm{mm}$ [47]. The pulse repetition rate is freely adjustable up to $30\,\mathrm{Hz}$. For the initial setup the first harmonic with a wavelength of $532\,\mathrm{nm}$ and about $35\,\mathrm{mJ}$ per pulse is used to work with higher photon energies and in the visible range making beam adjustments easier. This corresponds to a power density of about $1 \times 10^7\,\frac{\mathrm{W}}{\mathrm{cm}^2}$ as direct output. Focusing the beam to $500\,\mu\mathrm{m}$ would achieve the required power density with $T_D \approx 6 \times 10^8\,\frac{\mathrm{W}}{\mathrm{cm}^2}$. By focusing down even more, the laser can be operated at less power improving lifetime while leaving reserves if more power is required in the future. For the initial testing of the source, the produced ions will have to observed and identified. The devices and theory required to do this are summarized in the next section.

3.2 Ion detection schemes

3.2.1 Micro-channel plate

A micro-channel plate (MCP) [48] usually consists of a plate with a multitude of small tubes, called channels, that pass through it with a slight angle. The surface of the channels is coated with a semiconducting material. If any charged particle or photons with high enough energy hit the surface in one of those channels, secondary electrons are produced. Due to an applied voltage, these are accelerated and hit the surface of the same channel again creating a cascading (or avalanche) effect, multiplying the number of electrons as shown in figure 8. Those are then further accelerated and hit a detector unit which can be either a metal plate (called anode) to measure the current or, as one possibility to achieve spatial resolution, a phosphor screen that starts fluorescing due to the electron impact. If the phosphor screen is monitored by a fast camera, the impingement point can be observed.

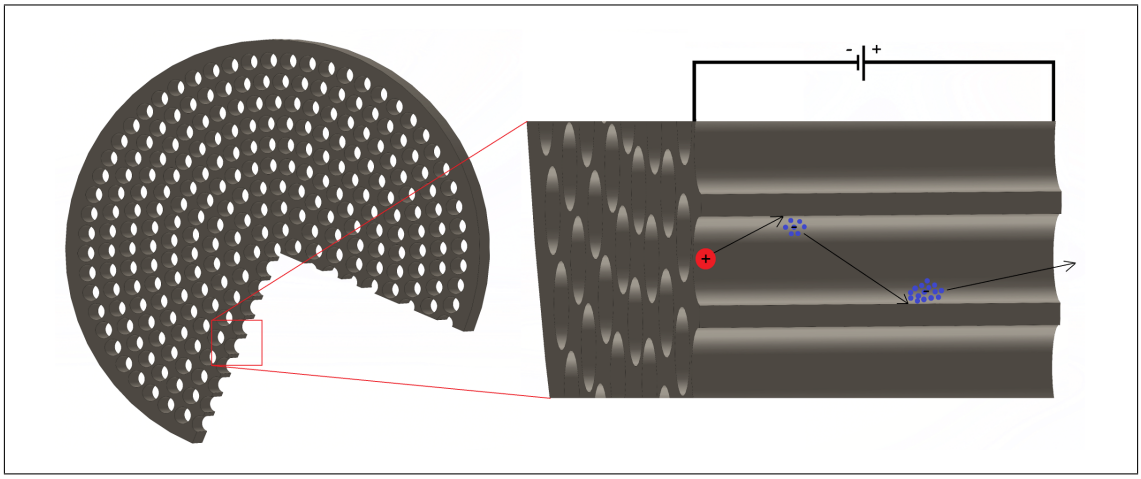

Figure 8: Schematic view of an MCP. On the right side the operating principle is illustrated with a positive ion (red) producing secondary electrons (blue) which then hit the wall again and so on. Upon leaving, the electrons are then accelerated onto either a metal anode or a phosphor screen to detect them.

For this setup an MCP in chevron design with two of such channel plates, each with a diameter of $d_{\mathrm{MCP}} = 36\,\mathrm{mm}$ is used, to further increase the detection efficiency. To this end, the plates are rotated 180° against each other so that the angles of the channels face in opposite directions.

It is possible to monitor the current hitting the phosphor screen simultaneously as the camera is observing it. With this, a time of flight spectrum can be measured while still having a spatial resolution of the ion beam. It is quite difficult, however, to estimate the number of ions from the current observed on the phosphor screen due to the not well

known amplification factor and detection efficiency, which is dependent on energy and mass of the ions as well as applied voltages [48, 49]. To measure the ion beam current, a Faraday cup will therefore be used.

3.2.2 Faraday cup

A Faraday cup normally consists of a set of a small cup and a ring electrode, the so called suppressor, in front of it. Ions hitting the cup will charge it up and a current will be measurable. Since the ions hitting the cup material may produce secondary electrons, the suppressor electrode is held on a negative potential U_{repel} to keep those electrons inside the cup and prevent an systematic error in the current measurement by additionally lost electrons. Because there is no unknown amplification used contrary to an MCP, this setup provides a direct measurement of the ion current, allowing a good estimation of the number of ions produced later on. A schematic overview is given in figure 9 a), the actual cup used is shown in figure 9 b).

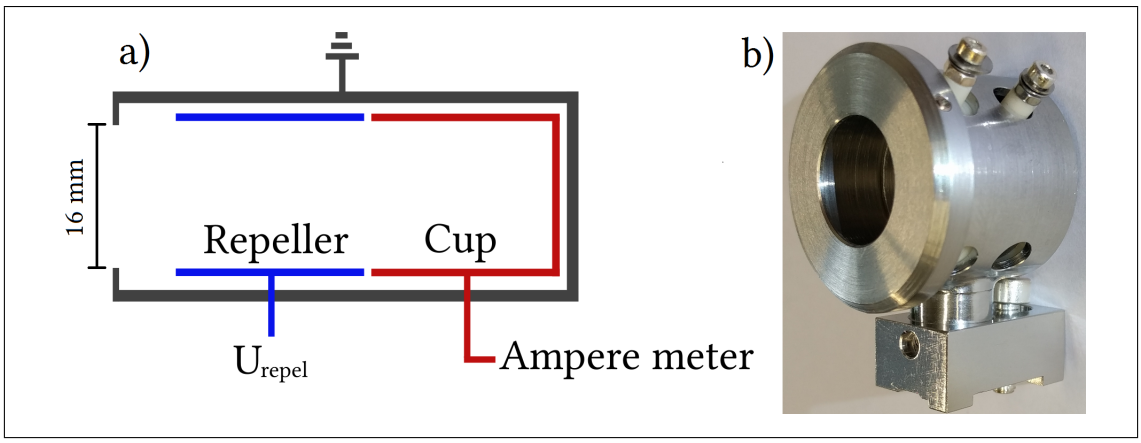

Figure 9: Schematic view of a Faraday cup on the left side (a) with the repeller electrode and the cup inside a grounded housing. The right side (b) shows the Faraday cup as used in the experimental setup.

3.2.3 Time-of-flight spectroscopy

The ions are produced in a region with a high potential and are accelerated towards either Faraday cup or MCP. After leaving the acceleration region, they will have the total energy E which corresponds to the sum of the potential energy in the acceleration region and their kinetic energy after production. The starting energy is known only with an uncertainty due to the exact starting position being unknown after the plasma expansion. The thermal energy adds another uncertainty. Since the combined uncertainty

is estimated to be small compared to the total energy, an identification of the species can be achieved by an analysis of the time-of-flight (TOF) spectrum. Neglecting the energy difference for the ions and using E as their average energy, the TOF is only dependent on the masses of the ions. This allows an identification, if the time resolution is high enough to resolve the TOF differences. Assuming an ion with constant velocity and therefore neglecting the initial acceleration time, causes an error of less than 2%, small enough to be neglected for this estimation. This results in the TOF t to be

$$t = s\sqrt{\frac{m_{ion}}{2E}} \quad , \tag{3.1}$$

with s being the drift distance of about $1.8\,\mathrm{m}$ to the MCP, m_{ion} being the ion mass and $E \approx 2.3\,\mathrm{keV}$ the ion energy which will be used for the extraction. This results in an estimation of $t_{Be} \approx 8.1\,\mu\mathrm{s}$ for beryllium and $t_{Al} \approx 14\,\mu\mathrm{s}$ for aluminum, which is the main contaminant as will be explained in section 3.3, due to the factor $\sqrt{m_{Al}/m_{Be}} = \sqrt{3}$. A time resolution in the low $\mu\mathrm{s}$ range is therefore required. This is possible for both, MCP and standard oscilloscopes, making an identification of ion species using TOF spectroscopy possible.

3.3 Ion extraction

To be able to trap the $^9Be^+$ ions in the cryogenic Penning trap after their transport through the beamline, their energy has to be lowered from about $2.3\,\mathrm{keV}$ to at least $1\,\mathrm{keV}$. This is achieved by a drift tube just above the cryostat (see figure 7) after the transportation path through the beamline of about $3\,\mathrm{m}$. Due to this long path, special care has to be taken to assure that the ions are well focused in time and space. The drift tube is on a potential below the energy of the ions. Upon entering the drift tube, the ions are slowed down. Once they are inside the homogenous field region in the tube, the voltage is pulsed down, lowering the energy of the ions inside to the difference between the energy of the arriving ions and initially applied voltage. To be able to do this and provide means of selection, the ions have to be bunched since only those inside the field region of the drift tube are slowed down and become trappable afterwards. Furthermore, other ion species should be separated in their TOF from the ions of interest such that the corresponding spatial distance is greater than the spread of the electric field of the drift tube. This will keep them on a high energy and prevent them from being trapped. This has to be the case after the beryllium ions are slowed down by entering the drift tube while the aluminum ions still have their initial energy, causing the separation to become smaller.

The length of the drift tube is $49.5\,\mathrm{cm}$ with grounded electrodes on both sides, setting the field region to essentially the same size. As the target to be used consists of $62\,\%$ beryllium and $38\,\%$ aluminum (mass percentages for AlBeMet®, material stated to be *commercially pure*) [50], this is the main contamination of ions to be considered when designing the ion extraction system.

To estimate if a separation is possible, the time required for the slowest beryllium ions to be $10\,\mathrm{cm}$ inside the drift tube is calculated, with the voltage of the drift tube assumed to be $500\,\mathrm{V}$ below the ion extraction voltage. The position of the fasted aluminum ions at that time has to be well before the drift tube. A SIMION® simulation shows that the position of the fastest aluminum ions is found to be at $1.64\,\mathrm{m}$ with the slowest beryllium ions being at $2.6\,\mathrm{m}$ – already $10\,\mathrm{cm}$ inside the pulsed drift tube. This estimation is done with the typical extraction voltages used for the aluminum-beryllium target, as will be discussed in chapter 5. The drift tube can potentially be set even lower, as the capture section of the trap allows voltages up to about $1\,\mathrm{kV}$. This would result in an increased beam quality and an even higher separation from the aluminum ions.

The possible transverse diameter of the ion beam is mainly limited by the aperture of the two quadrupole benders. Those are used to bend an ion beam by $90°$ each and feature a $10\,\mathrm{mm}$ aperture, which restricts the maximum size due the corresponding field shape [36], requiring the beam to be smaller than that for an effective transmission.

3.4 Wiley-McLaren setup

To extract the produced ions, a permanent extraction voltage is applied on the acceleration electrodes. As the laser induced plasma is produced in front of the target but thermally expands, the ions will be in different positions once cooled down and are not accelerated from the same starting potential. This results in an energy spread after the acceleration stage, which leads to the lower energy ions with the shorter extraction path being overtaken at the time focal point T_d by the higher energy ones with a respectively longer path. This effect is shown in figure 10.

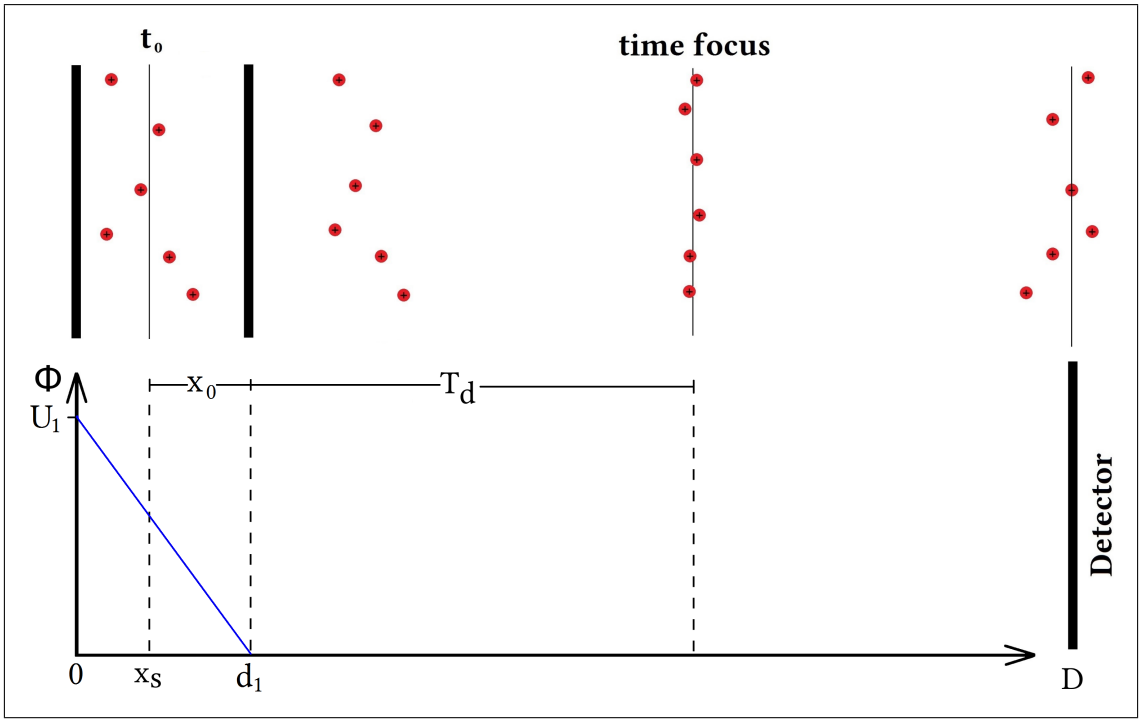

Figure 10: Upper panel: Ions (red) are produced on the mean starting position x_s at time t_0. Ions produced on a higher potential with the longer path overtake the ones produced at a lower potential with the shorter path at the time focal point T_d. This point is dependent on the electric field strength in the region from 0 to d_1. The ions arrive unfocused at the detector D. The lower panel shows the electric potentials.

The only free parameter is the total energy that depends on the applied voltage U_1 on the target electrode (position 0). Since changing it would directly effect the radial distribution as well as the time required for extraction and transportation, the possible changes are highly restrained and only allow for time focal points a few cm behind the extraction section – for this setup with an extraction voltage of $U_1 = 2.3\,\mathrm{kV}$ and ions distributed around the starting point of $x_s = (1.5 \pm 1.5)\,\mathrm{mm}$, the time focal point would be $T_d \approx 2.3\,\mathrm{cm}$ resulting in the ions arriving at the detector D being spread out in time.

The Wiley-McLaren setup [51] provides a solution by adding an additional acceleration stage that allows to correct for the error of the starting point and make the time focal point adjustable without varying the total energy, as illustrated in figure 11.

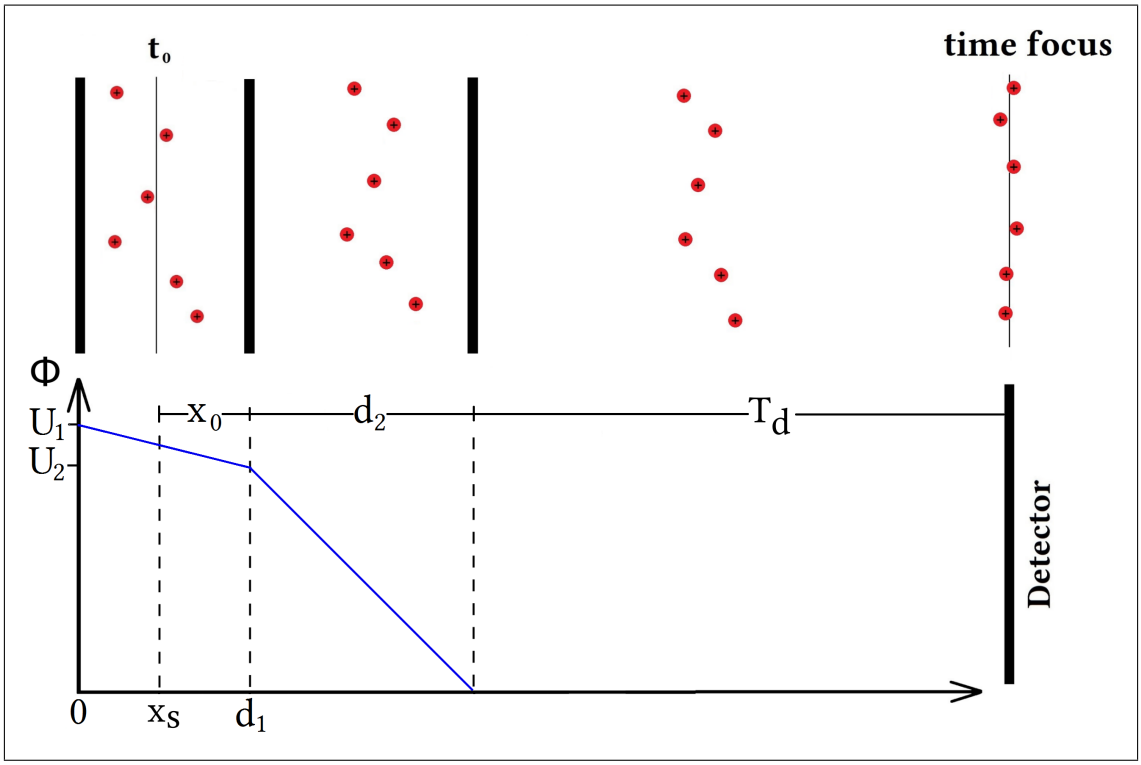

Figure 11: The upper part shows the extraction unit with the black bars indicating the electrodes. The lower part shows the potentials applied in the different sections. The ions (red) are produced at mean starting position x_s at time t_0. U_1 is the same as before to keep the total energy unchanged. U_2, the voltage of the second electrode, can define a ratio of the electric field strengths in the two sections. Changing this ratio allows to shift the time focal point T_d onto the detector plane D.

Calculating the TOF from the mean starting position x_s and minimizing the deviations for starting point shifts $x_s \pm \Delta x$ yields the time focal point T_d [51], given as the distance after leaving the second section, as

$$T_d = 2x_0 \cdot \sqrt{k_0^3} \left(1 - \frac{d_2}{x_0} \frac{1}{k_0 + \sqrt{k_0}} \right) \tag{3.2}$$

where

$$k_0 = \frac{x_0 E_1 + d_2 E_2}{x_0 E_1} \quad . \tag{3.3}$$

$E_1 = {}^{(U_1 - U_2)}/_{d_1}$ is the electric field in the first section and $E_2 = {}^{U_2}/_{d_2}$ in the second

section with U_1 and U_2 being the voltages applied to the corresponding electrodes. x_0 is the distance from the mean production point x_s to the second electrode, d_2 is the distance between the second and the third electrode.

Once the electrode distances d_1 and d_2 are fixed U_1 gives the total ion energy and U_2 can be used to control the position of the time focal point as follows from equation (3.2) and (3.3).

This setup also lowers the the energy spread caused by the starting position, since the electric field in the first section is significantly weaker compared to a single stage setup. Therefore, the position dependence of the energy is smaller, resulting in an overall smaller energy distribution. However, this does not correct for the time-spread caused by ions with an initial velocity in the direction opposite of the extraction direction. These are slowed down and then turned around, creating a temporal spread that increases the smaller E_1 becomes, since the turn around time increases. Therefore, depending on the spatial spread and kinetic starting energy, an optimum has to be found where the deviation due to these counteracting effects is smallest.

3.5 Spatial focusing

To focus and steer the beam after the extraction, a system of three einzel lenses is used. For a single such lens, three ring electrodes are commonly used. To the center electrode a high voltage is applied while the outer ones are grounded. If multiple such lenses are combined, they can share the ground electrodes resulting in a set up alternating between grounded and high voltage electrodes. Additionally, by segmenting the ground electrodes into four parts, an adjustment of the beam direction with one of the segmented electrodes or a positional shift when using a combination of both is possible.

The principle of operation of an einzel lens is shown in figure 12. The lens can be operated with positive or negative voltage to focus the ions. In practice, when working with positive ions, negative voltages are preferable. Due to the resulting energy gain in the lens, aberration effects are not as strongly pronounced as with positive voltages, where the ions are momentarily slowed down during the focusing. This increases the radial spread, causing ions to move further from the center where field inhomogeneities are stronger pronounced. This effect can be seen in figure 12, where the beam initially widens in the positive lens, whereas it becomes gradually smaller in the negative one. Therefore, a decelerating (positive) lens will always cause higher aberrations than an accelerating (negative) one when working with positive particles. However, positive voltages can achieve a stronger focus with the same absolute voltage, which make them useful for operations with voltage limitations.

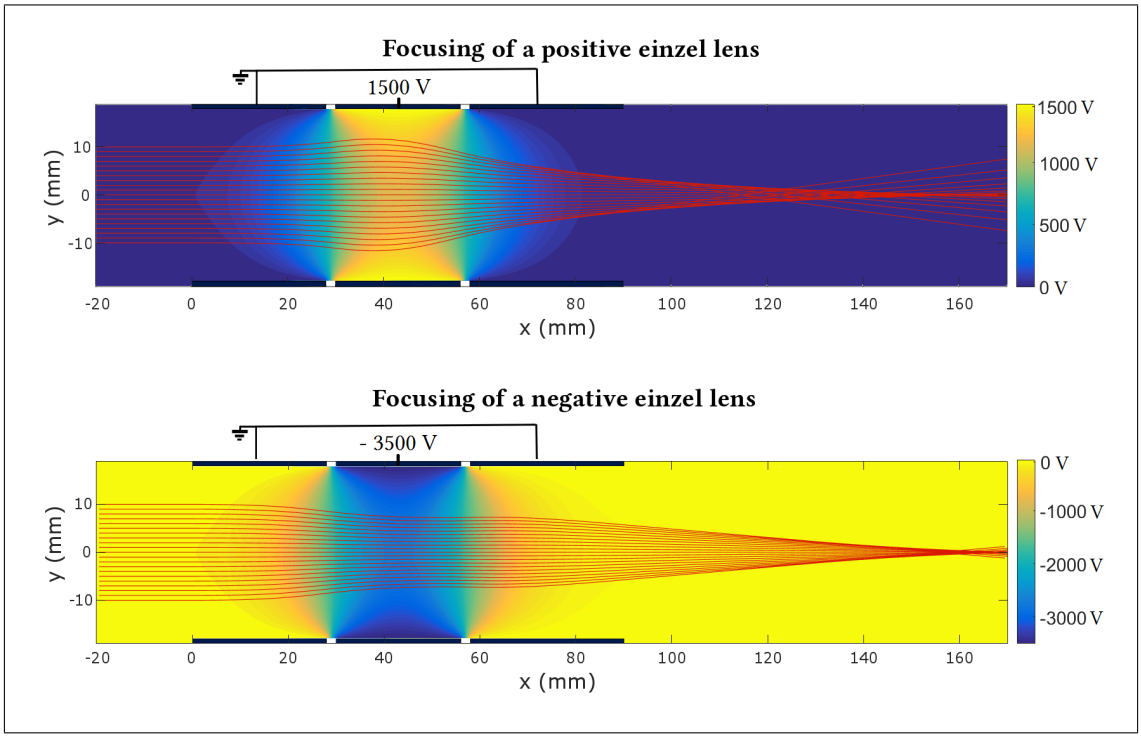

Figure 12: Simulation of the focusing of an einzel lens. The single positively charged ions are initially started as a parallel beam with an ion energy of 2 keV. A similar focus of about 160 mm is achieved with 1500 V (upper picture) and −3500 V (lower picture) but fringe effects are already visible for the positive lens, resulting in a better focus for negative voltages. The field and the ion trajectories have been calculated with SIMION® and been replotted with MATLAB®.

3.6 Design of the extraction unit

To combine both, Wiley-McLaren acceleration stage with three einzel lenses, a SIMION® study has been performed to optimize the ion extraction for different starting parameters by comparing different designs. From this, the design of the extraction unit could be concluded, while giving a good estimation of the required voltages and the expected extraction path. To be able to do this, an initial spatial ion distribution as well as the kinetic energy distribution has to be assumed, since these are dependent on the experimental parameters such as laser power density, wavelength, pulse length and target material. An in-depth study concerning properties of laser induced plasmas including a compilation of different materials and laser parameters has been performed by Zhang *et al.* [52]. From this can be concluded that typical laser induced plasmas show initial temperatures starting from 4×10^3 K up to 3×10^4 K which quickly cool down on a timescale of a few 100 ns up to over 2 µs. Transferring this to beryllium, a worst case energy of 4 eV is assumed that corresponds to a temperature of about 3.1×10^4 K.

If the plasma would keep expanding for about $500\,\mathrm{ns}$ while gradually cooling, an expansion of about $4.5\,\mathrm{mm}$ can be estimated. Since both, energy and cooling time are likely to be overestimated, a uniform distribution from $1\,\mathrm{mm}$ to $4\,\mathrm{mm}$ is assumed.

For the spread orthogonal to the extraction direction, a uniform distribution from $-1.5\,\mathrm{mm}$ to $1.5\,\mathrm{mm}$ with 0 being the laser spot position is chosen since ions further away will be hitting the second electrode anyhow.

The resulting energy spread is now almost completely due to the different starting potentials which contributes to $^{\Delta E}/_{\Delta x} = \pm 25\,\frac{\mathrm{eV}}{\mathrm{mm}}$. The ions are assumed to keep the thermal energy of $4\,\mathrm{eV}$ during the complete extraction process with the direction being uniformly distributed. As this already includes all energies in beam direction from $0\,\mathrm{eV}$ to $4\,\mathrm{eV}$, a additional distribution of the energies does produce different results and can be neglected, as it is small compered to the starting potential difference anyway.

The resulting simulated extraction path is illustrated in figure 13. The extraction voltages here are $\mathrm{U_{Acc1}} = 2300\,\mathrm{V}$, $\mathrm{U_{Acc2}} = 2000\,\mathrm{V}$ and $\mathrm{U_{Acc3}} = 650\,\mathrm{V}$. Unlabeled electrodes are grounded.

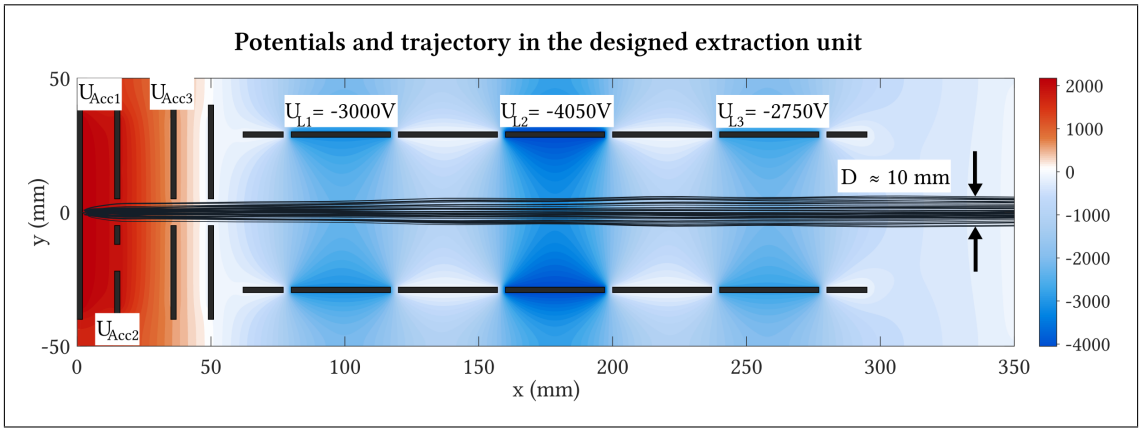

Figure 13: The black bars indicate electrodes with the corresponding voltage applied, unlabeled electrodes are grounded. The dark gray lines indicate the $^{9}\mathrm{Be}^{+}$ ion trajectories with the given starting parameters. The hole in the second electrode is used for laser access and will be discussed in the next section.

The focal point is chosen to be at $\mathrm{x} \approx 1.2\,\mathrm{m}$ which is just after the first quadrupole bender with a simulated focal width of about $8\,\mathrm{mm}$. With the next set of ion optics at $\mathrm{x} \approx 1.5\,\mathrm{m}$ after the second quadrupole bender this allows for a transmission through both benders which feature an aperture of $10\,\mathrm{mm}$ while the beam can be refocused afterwards.

The extraction voltages $\mathrm{U_{Acc1}}$, $\mathrm{U_{Acc2}}$ and $\mathrm{U_{Acc3}}$ are calculated to produce a time focal point on the MCP plane of the offline test setup in about $1.8\,\mathrm{m}$ distance where the TOF spectra is recorded. For the final setup the voltages will have to be slightly adjusted to achieve a time focus on the position of the drift tube.

With voltages available from $-6\,\mathrm{kV}$ to $6\,\mathrm{kV}$ from a CAEN crate, which is explained in more detail in the chapter on the experimental setup (see section 4.2.1), there is still room to increase the ion energy which would result in a lower radial size due to the smaller extraction angle.

3.6.1 CAD-Design

The schematic electrode structure as simulated has been designed as a machinable set of lenses and electrodes in the CAD program SolidWorks®. The complete extraction unit is shown in figure 14. The electrodes are machined in the institutes own workshop and are made of stainless steel. The electrical insulators are externally manufactured ceramics with the trade name Macor®.

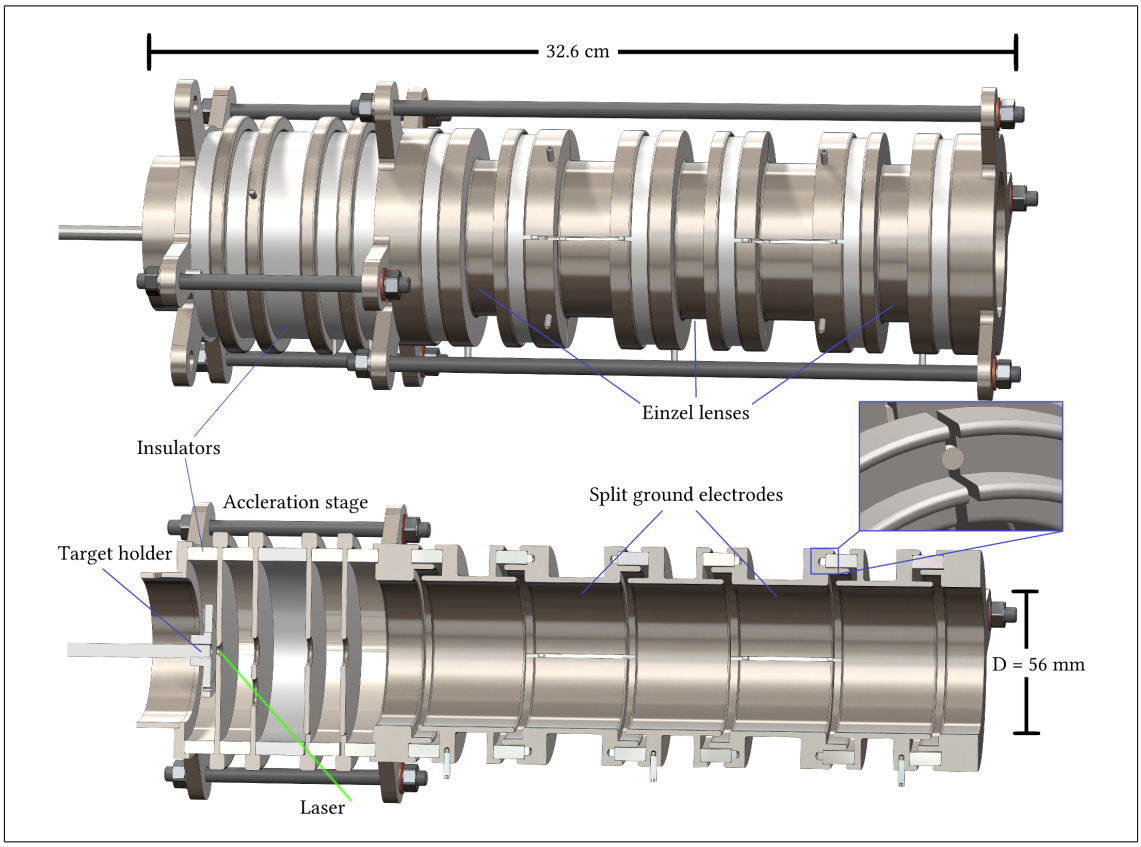

Figure 14: Illustration of the extraction unit as a full view and as cut along the center of the ion extraction direction. The target is placed behind the first electrode with the laser entering the extraction unit from below in an angle of $45°$. Cuts in the insulating rings and the holes in the second and third acceleration electrode allow optical access from below to reach the target through the central hole in the target electrode. The two central ground lenses are split into four parts with spacing insulators to hold them in place as shown in the detailed view on the right hand side.

The hole in the second electrode to allow access of the laser onto the target has been simulated in SIMION® to assure that the field distortions caused by it do not affect the ions along the central axis as shown in figure 13. For all typical extraction voltages this was found to cause less than a $1\,\mathrm{V}$ change in the potential on the central axis thus being completely negligible. The overlapping shape of the einzel lenses and their corresponding grounded electrodes assures that the isolators cannot be hit by ions which could otherwise charge them and cause field distortions. Additionally, the design allows a bake out of the unit up to $300\,^{\circ}\mathrm{C}$ due to the expansion coefficient of the ceramics being smaller than that of the steel. Since the steel encloses the ceramics from the outside, it can expand without breaking.

The split ground lenses allow individual voltages for each of the four segments which can in combination of the two be used to either slightly shift the beam or adjust the angle if necessary. The single parts are being held in place by small cylindrical insulators that prevent the segments from touching each other as shown in figure 14. The target is in electrical contact with the first electrode and additionally connected to the same voltage, assuring the same potential for both.

3.6.2 Vacuum chamber

The vacuum chamber to house the extraction unit has to provide means of laser access, enough high-voltage feedthroughs (SHV) to connect all electrodes, enable target replacement and position adjustments while leaving enough space for the turbo pumps and vacuum sensors. The central part of the chamber is made of two three-way crosses which feature ConFlat (CF) 160 flanges on the axis of the extraction unit and CF-100 flanges on the other two. CF flanges are commonly used for UHV conditions in the range of down to $10^{-13}\,\mathrm{mbar}$. Due to the sealing being achieved by metal rings, the complete chamber including the extraction unit can be baked out to reduce outgassing and improve the achievable vacuum. The parts used to build the chamber are shown in figure 15.

Since the target material will be ablated by each laser shot, the surface structure will change. To prevent decreasing efficiency of the ion yield per shot, the spot hit by the laser has to be changed. To achieve this, a motorized two dimensional linear stage is used to reposition the target automatically. The stage allows a reposition by moving the target inside a CF40 bellow, giving access to an area of about $6\,\mathrm{cm}^2$. With estimated spot diameters in the range of $200\,\mu\mathrm{m}$ and a resolution of about $25\,\mu\mathrm{m}$ per motor step, this allows for several thousand different positions before the target has to be exchanged.

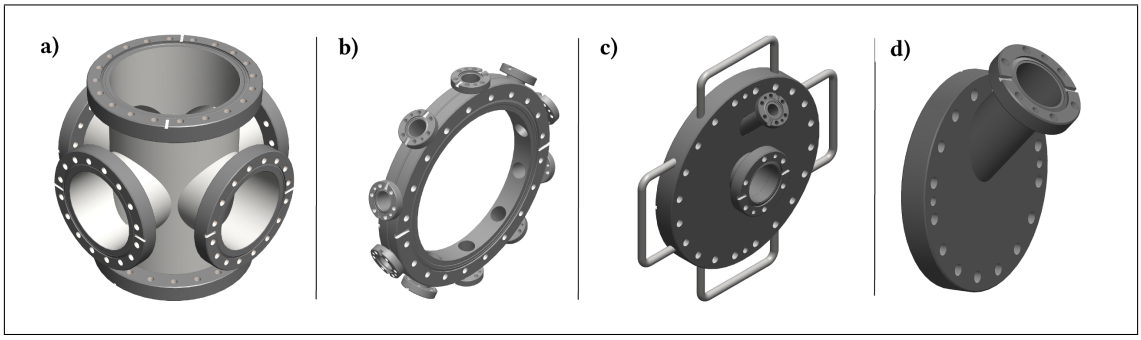

Figure 15: a) three-way cross as available from VAb [53] b) custom design of a spacing flange with 10 radial CF-16 ports used for voltage feedthroughs. c) custom front flange with the central port for target insertion and the $45°$ port for laser beam monitoring. d) custom bottom flange with a $45°$ view-port to allow access for the laser.

The laser can pass through the setup and exit through the monitoring port when the target holder is moved to a specific position. This is achieved by it featuring a small slit that allows to shoot the beam through and allow easy adjustments. The actual target material is clamped onto the holder through the three holes. The design of the target holder is shown in figure 16.

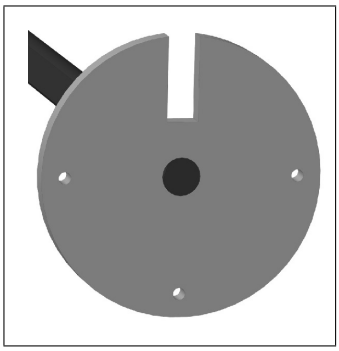

Figure 16: Target holder

For pumping the chamber a turbomolecular pump (EDWARDS Stpa803cv[54]) is used. It features a pumping speed of $800\,\frac{\mathrm{L}}{\mathrm{s}}$ for nitrogen and should achieve a pressure of at least $10^{-9}\,\mathrm{mbar}$ if no restricting leaks are present [54]. The vacuum is monitored by an ionization vacuum gauge by Pfeiffer Vaccum. The complete CAD model of the LIS is shown in figure 17.

The lens, which is required to focus the beam onto the target, is placed directly in front of the view-port for laser access. This allows an easy adjustment of the focal point by keeping all optical elements outside of the vacuum. Additionally, sputtering of the ablated material onto optical elements other than the view-port is prevented, which increases the operation time before maintenance is required. The distance between the view-port and the target is $d = 28\,\mathrm{cm}$, requiring a plano-convex lens with a focal length $f = 30\,\mathrm{cm}$.

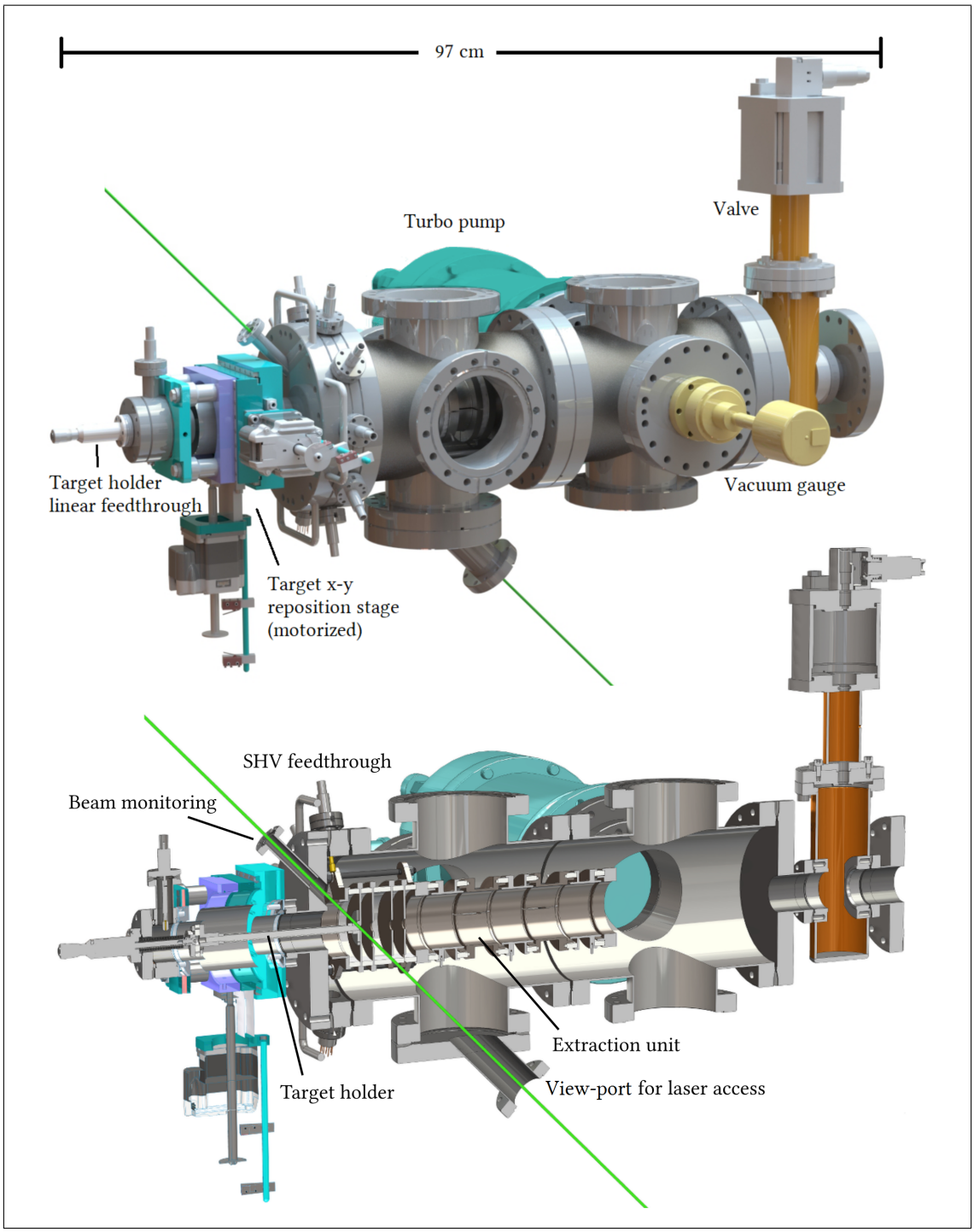

Figure 17: A complete model of the LIS. The combination of the two crosses houses the extraction unit which is screwed onto the front flange as shown in figure 15 c). Additionally, a pressure gauge to measure the pressure in the chamber as well as a valve to close off the chamber is shown. The lower part shows a cut along the ion extraction direction. The mounted extraction unit can be seen as well as the illustrated laser path.

4 Experimental setup

4.1 Extraction unit and targets

The extraction unit is built by stacking the different electrodes seperated by insulators. They are held in place by the end pieces pressing them together via threaded rods. The acceleration and lens part are independently fixated for an easier assembly or if maintenance is required. All electrodes are connected with Kapton® insulated copper wires with additional ceramic tube insulators at critical positions of the cable. Care is taken to assure sufficient space between HV-wires and grounded parts. To connect the cables to the electrodes and feedthroughs push-pins made of copper-beryllium are used. For the eight-pin feedthrough, as seen in figure 18 in the upper left corner, the connection is made by laser-welding the copper wires directly to the feedthrough pins. This connection is then insulated by ceramic tubes. The completely cabled stack, aligned to about $\pm 1°$, is shown in figure 18.

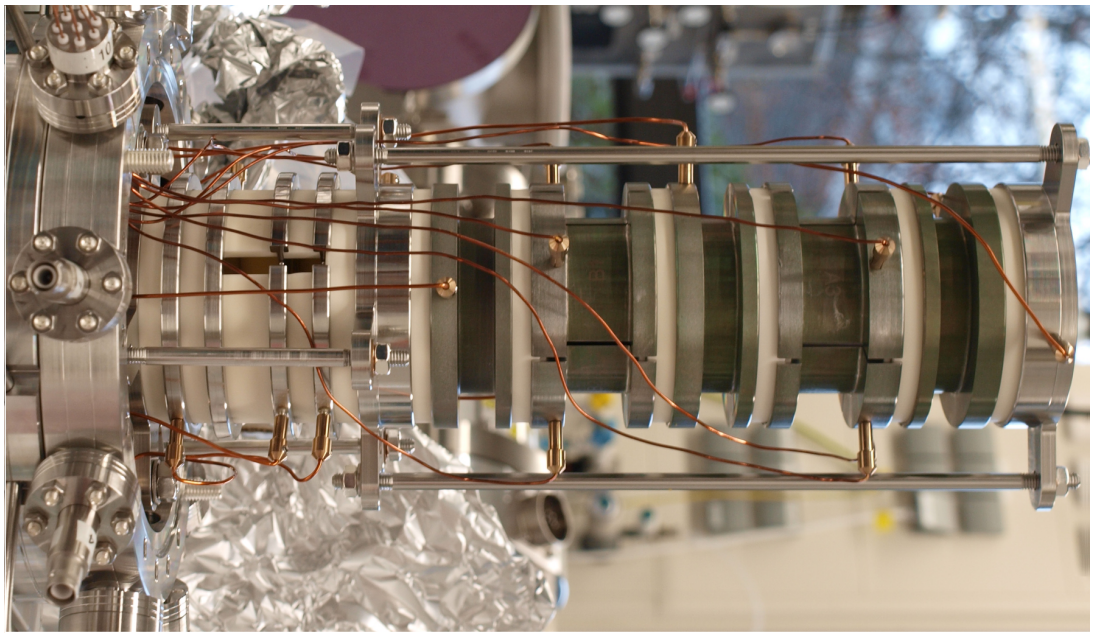

Figure 18: The assembled, wired and mounted extraction unit. The slit in the electrodes and insulators of the acceleration section are for laser access and can be seen on the left side.

The greenish tint of the larger lens electrodes was caused by a leak which resulted in a pressure of 10^{-3} to $10^{-2}\,\mathrm{mbar}$ during the bake-out for $3\,\mathrm{h}$ at $900\,°\mathrm{C}$. This most likely caused an oxidation of the chromium alloy content of the steel resulting in the green chromium(III)-oxide Cr_2O_3 [55]. To avoid potential field distortions, caused by

the electrical non-conducting oxide layer, the inner parts of the affected electrodes were polished again as a precaution even though measurements on the outside didn't show any reduced conductance. For this a layer of $50–100\,\mu\mathrm{m}$ thickness had to be removed.

As a first target, a copper foil is clamped to the target holder combined with stripes of copper-beryllium $(98\% : 2\%)_{\mathrm{mass}}$ and aluminum that are wrapped around the copper sheet (see figure 19 (a)). The second target has been produced with a similar copper foil as a basis on the target holder. However, this time pieces of carbon, aluminum and aluminum-beryllium are glued on the copper sheet with a two-component epoxy glue [56] as shown in figure 19 (b). The glue was kept under a vacuum of about $10^{-2}\,\mathrm{mbar}$ for the first half-hour after mixing the components until no boiling could be observed anymore to allow an out-gassing before its usage in the vacuum chamber. The processing time of the glue is given as $90\,\mathrm{min}$. The target was dried for $12\,\mathrm{h}$ and mounted in the setup afterwards.

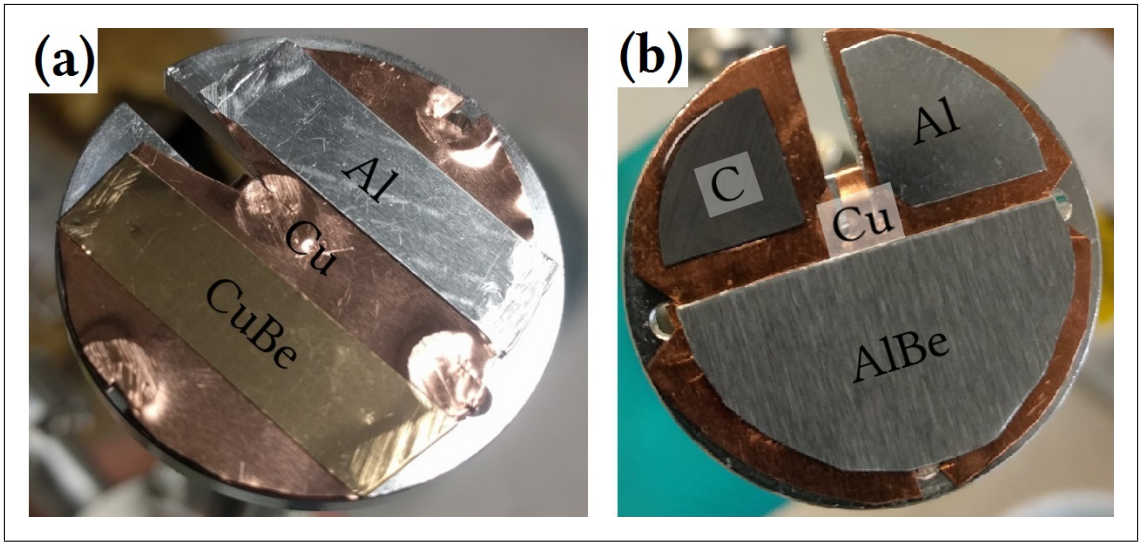

Figure 19: The two targets used, (a) with copper, aluminum and copper-beryllium and (b) with the glued carbon, aluminum and aluminum-beryllium. For details see text.

4.2 Offline setup

The offline setup was built for the initial testing and characterization of the LIS. The laser is placed in a closed box made of black anodized aluminum sheets for safe operation. To monitor the laser power, a beam-splitter is used to reflect a small percentage of the laser beam onto a power-meter (Thorlabs ES111C [57]). A schematic overview of the offline setup is shown in figure 20.

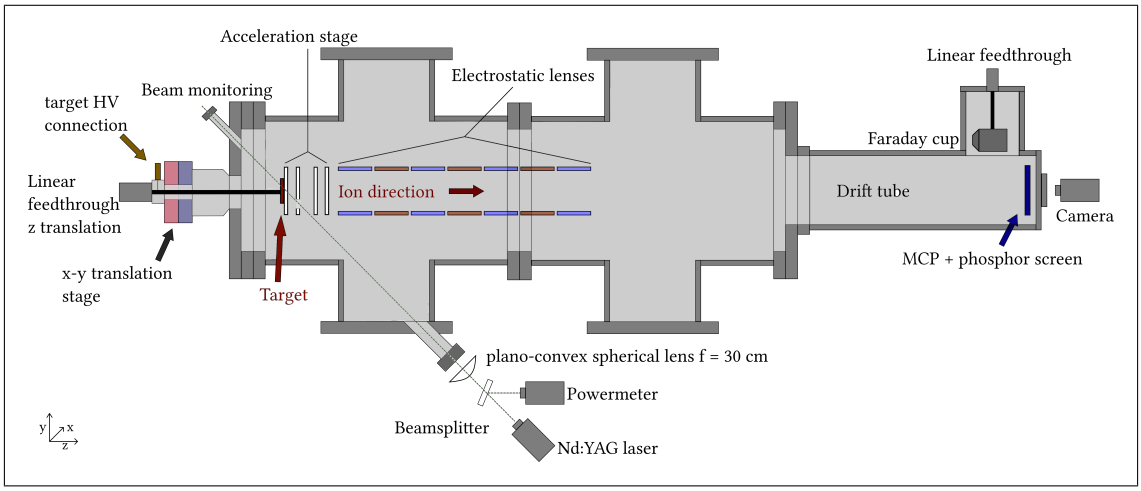

Figure 20: Schematic overview of the offline setup. The ions get extracted towards the right (z-axis). The drift tube length is changed for two different setups, first amounting to a total of $(0.85 \pm 0.01)\,\mathrm{m}$ between target (red) and MCP (blue), later-on to a distance of $(1.77 \pm 0.01)\,\mathrm{m}$.

For the initial tests with the first target, the total distance from target to MCP is only $x = (0.85 \pm 0.01)\,\mathrm{m}$ due to a short drift tube. For further testing, this distance is increased to $x = (1.77 \pm 0.01)\,\mathrm{m}$ by adding a longer drift section. Additionally, the Faraday cup is added to allow for current measurements of the ion beam intensity. The camera (AlliedVision Gc655) is placed behind the view-port to monitor the image produced by the phosphor screen. At the same time, the electrical signal of the phosphor screen can be measured by connecting an oscilloscope (Tektronix MSO 2024) to produce the TOF spectra. When the Faraday cup is used instead, it is connected to a pico-ammeter (Keithley 6514) to measure the ion current. The final offline setup with all components assembled, including the Faraday cup and the long drift section, is shown in figure 21.

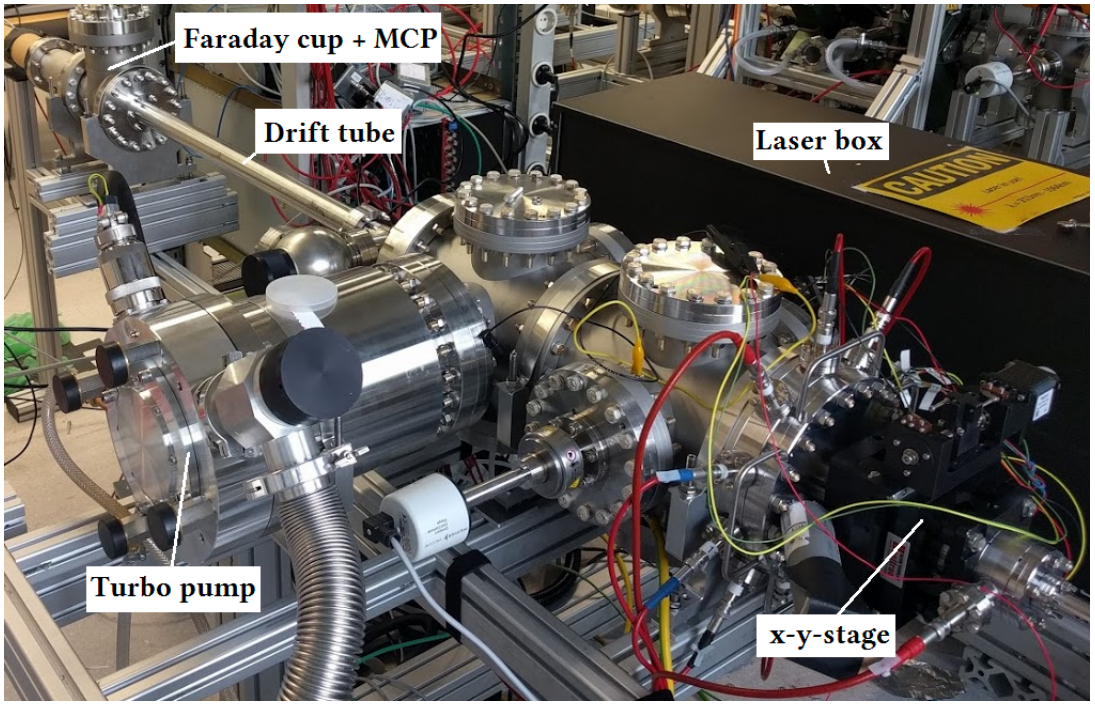

Figure 21: The offline setup used for testing the LIS. The Faraday cup is in the cross in the upper left corner with the MCP and camera directly behind. The ions source, consisting of the two crosses with feedthroughs in the front, can be seen as well. The total distance from target to MCP is $(1.77 \pm 0.01)\,\mathrm{m}$.

4.2.1 High-voltage supply

A CAEN crate [58] is used as high-voltage supply. It features 24 channels, of which 12 provide $0\,\mathrm{V}$ to $6\,\mathrm{kV}$ and 12 provide $0\,\mathrm{V}$ to $-6\,\mathrm{kV}$ with a current of up to $200\,\mu\mathrm{A}$ each. The connections are made by SHV connectors directly to the setup. Due to the noise present on the outputs of the CAEN crate, which made a measurement of the MCP signal impossible, the channels supplying the front- and back-plate of the MCP as well as the phosphor screen are filtered with a low-pass filter. The individual voltages used are $U_{\mathrm{front}} = -1.6\,\mathrm{kV}$ for the front-plate, $U_{\mathrm{back}} = 200\,\mathrm{V}$ for the back-plate and $U_{\mathrm{screen}} = 2.2\,\mathrm{kV}$ for the phosphor screen. Additionally, a connected capacitor assures that the voltage is stabilized by providing the current produced by the secondary electrons leaving the plates.

4.3 Expected parameters

The TOF of the produced ions is calculated from the average starting point in the first section as shown in figure 11. For ions starting in the direction opposite to the extraction direction, an additional turn-around time t_{turn} has to be considered:

$$t_{\text{turn}} = \frac{m_{\text{ion}} d_1}{q\Delta U} \sqrt{\frac{2E_{\text{therm}}}{m_{\text{ion}}}} \quad . \tag{4.1}$$

This causes a maximum TOF difference of $2 \cdot t_{\text{turn}}$ in the TOF spectrum, which for $^9\text{Be}^+$ ions with a voltage difference $\Delta U = 200\,\text{V}$ and an assumed thermal energy of $E_{\text{therm}} \approx 4\,\text{eV}$ as used in chapter (3.6) results in $t_{\text{turn}} \approx 50\,\text{ns}$, scaling with $\propto \sqrt{m_{\text{ion}}}$ for other ions.

The TOF difference due to the thermal kinetic energy is smaller. By assuming a uniform starting direction, all energies between 0 to $4\,\text{eV}$ in extraction direction are accounted for. The difference between the fastest and the slowest ions amounts to only about $10\,\text{ns}$ when using a total energy of $2300\,\text{eV}$. Not included in the time-spread is the effect of ions being extracted at different times due to a gradually cooling plasma. This means, that the outer areas of the plasma might cool down faster, resulting in an earlier extraction time for ions produced there compared to the center of the ignited plasma. Cooling times for the complete cloud are typically in the regime of several $100\,\text{ns}$ which causes the biggest spread in the expected TOF spectrum. This results in an expected peak-width of several $100\,\text{ns}$ for beryllium ions while scaling up for higher masses due to the increased turn-around time and possibly longer cooling times for higher masses [52].

For ions not starting opposite to the extraction direction but at an arbitrary angle, the turn-around time is smaller. Since these ions will not follow a straight path to the MCP but follow are more complex trajectory due to their angle, the TOF difference for this is included in the performed simulations. Due to the initial uniform direction distribution (see section 3.6), this TOF difference is included as the standard deviation of the simulated flight-times.

5 Measurements and results

In the following, different measurements performed in the offline setup of the LIS are described and evaluated. Due to varying parameters of the experimental setup, an overview of the most important changes between the two different configurations used is given in the next section.

5.1 Overview of experimental parameters

Table 1 shows a general overview of the parameters used for the measurements presented in the following. It should be noted that the two experimental setups (listed as configuration 1 and 2) varied in drift length, voltages, target materials and measurement devices.

	Total drift length	U_{Acc1}	Target	Faraday cup	MCP
Configuration 1	$(0.85 \pm 0.01)\,\text{m}$	$1320\,\text{V}$	Cu, Al, CuBe	X	✓
Configuration 2	$(1.77 \pm 0.01)\,\text{m}$	$2300\,\text{V}$	C, Al, AlBe	✓	✓

Table 1: The table lists the most important parameters of the following measurements.

The given total drift length is the distance between target and MCP, the extraction voltage U_{Acc1} corresponds to the voltage on the first electrode and the target. The Faraday cup and MCP column indicate, if these detection devices are available for measurements in that configuration.

5.2 TOF measurements with the first configuration

The measurements performed with the first target are done with extraction voltages of $U_{\text{Acc1}} = 1320\,\text{V}$ and $U_{\text{Acc2}} = 1200\,\text{V}$ for the first and second acceleration electrode, respectively. This corresponds to the time focus being on the MCP plane, at a distance of $x_{\text{D}} \approx 85\,\text{cm}$ from the target. These voltages were both calculated and simulated (parameters as in section 3.6) in SIMION® with consistent results as shown in figure 22.

While the calculation gives the position of the time-focal point directly as a function of the second electrode voltage U_{Acc2}, for the simulation one has to determine the minimum in the TOF deviation at the required distance by scanning U_{Acc2}. From both methods a voltage of $U_{\text{Acc2}} \approx 1200\,\text{V}$ can be extracted.

For the first measurement, the signals resulting from the target materials of copper and copper-beryllium are compared. All settings, including voltages, laser parameters and sample time are the same for both materials. The measurement was performed on a spot that has been ablated for about $10\,\text{min}$ with a laser repetition rate of $30\,\text{Hz}$ and a

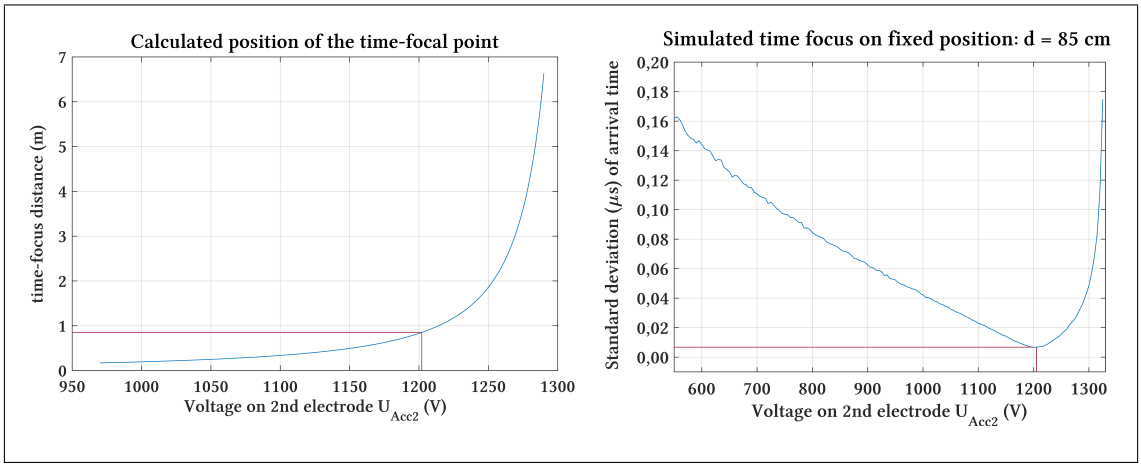

Figure 22: Both figures show the dependence of the time-focus on the second electrode voltage U_{Acc2} with a fixed acceleration voltage $U_{\text{Acc1}} = 1320\,\text{V}$. The left figure shows the calculation of the time focus position as derived in equation (3.2) for the Wiley-McLaren setup. On the right side, a simulation done with SIMION® for the distance of $x_{\text{D}} = 85\,\text{cm}$ is shown. The standard deviation of the TOF is plotted against the second electrode voltage U_{Acc2}.

pulse energy of $(2.86 \pm 0.06)\,\text{mJ}$ to get rid of possible surface contamination before the spectrum was recorded. The spectrum shows 256 recorded single shot spectra averaged by the oscilloscope.

The calculated TOF values of t_c are extracted from the SIMION® simulation. The errors are the combined standard deviations of the TOF resulting from the assumed initial distribution as discussed in section 3.6 and the uncertainty of the drift length. This is included by using the difference between the median TOF of separate simulations for a distance of $85\,\text{cm}$ and $86\,\text{cm}$ as standard deviation of the drift length. This yields the same result as using half the TOF difference between a simulation $84\,\text{cm}$ and $86\,\text{cm}$. The complete simulation is always performed for the used lens, extraction and MCP front-plate voltages. The measured TOF t_{m} is extracted by performing a Gaussian fit to the peak. The median corresponds to the measured value, the error is the standard deviation here as well. The time is measured relative to the trigger signal of the laser, which corresponds to the laser pulse being fired. The result is shown in figure 23 with the relative intensities scaled to compare to the maximum of the copper-beryllium spectrum with both measurements being corrected for their zero-level offset.

This is the first result from which the production of $^9\text{Be}^+$ ions can be concluded unambiguously. The only additional peak, when comparing to a pure copper target and a copper-beryllium alloy, matches the calculated TOF for beryllium. No other possible ions are expected close enough to the measured TOF to explain this signal. The agreement

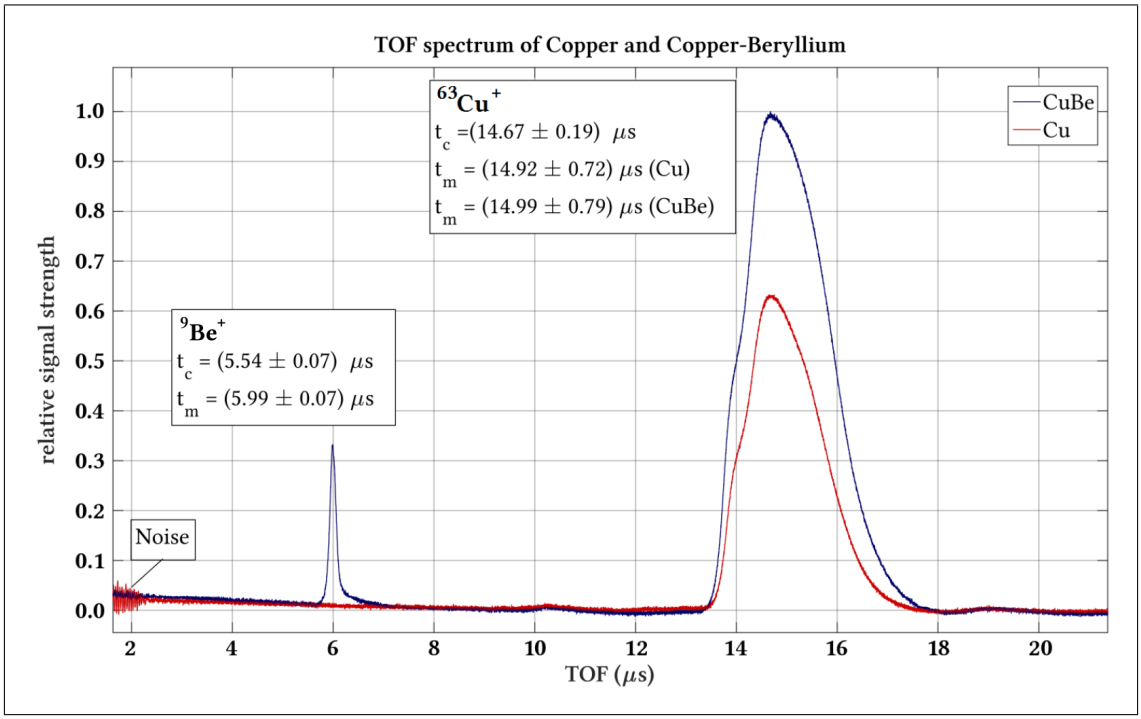

Figure 23: Shown is the TOF spectrum of copper-beryllium (blue) and copper (red) averaged from 256 single shot spectra. The signals are scaled relative to the copper peak of the copper-beryllium measurement. For details see text.

of the two copper peaks with each other should also be noted, having a very similar line shape with their TOF in perfect agreement. The peaks are expected to be slightly broadened since copper appears in two stable isotopes in nature, ^{63}Cu with an abundance of 69% and ^{65}Cu with 31%, respectively [59]. The resulting TOF difference is only about 220 ns though and cannot be resolved with the limited flight distance here. The slight deformation on the left side of the peak is found to be at about 14.1 µs and does not match this difference and thus corresponds to either an unidentified ion species or an electrical effect of the MCP.

Even though the percentage of copper in the target material is significantly higher than that of beryllium, with mass percentages of 98% and 2% respectively, the beryllium peak measures about 30% of the copper peak intensity. This might be due to a higher ionization rate or a higher ablation efficiency for single beryllium atoms compared to copper. Considering the ratios of atoms in the target material a peak intensity of only about 15% is expected.

The noise in the beginning of the spectrum is due to the trigger signal of the laser and is still visible when no ions are produced. This is checked by blocking the laser path into the setup which did not affect this signal.

The mismatch of the calculated TOF t_c compared to the measured t_m is due to the

at this point unknown systematic offsets. The leading contributions are the difference between the Q-switch trigger signal output of the laser, which is when a pulse should be emitted and the actual emission, and the cooling time of the plasma until the ions can be extracted. The measured delay of the better defined $^9Be^+$ peak, compared to the simulated value t_c, is (450 ± 99) ns.

To correct for the delay resulting from the laser, this has subsequently been measured with a photo diode [60]. Due to the fast rise time (< 40 ps), the pulse length of the laser can be extracted from this measurement as well. The measurement is shown in figure 24.

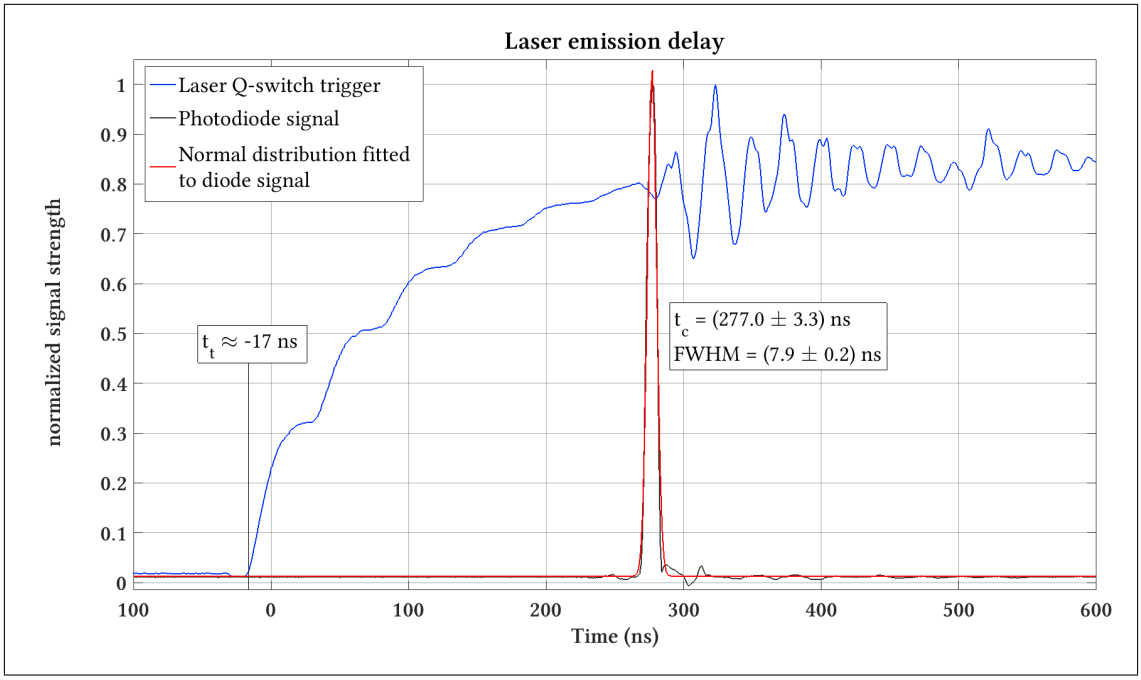

Figure 24: The measurement shows the emission delay of the laser. The blue curve is the Q-switch trigger signal coming directly from the laser control unit. The black curve is the measured signal of the photo diode with a fitted Gaussian to extract the exact time and the FWHM.

Because of the dependance on the trigger level, which defines the zero point of the measurement, all following spectra are corrected to the beginning of the slope as marked. Here, this trigger time is $t_t \approx -17$ ns. This results in a total delay of $t_d \approx (294 \pm 5)$ ns with the uncertainty resulting from the trigger shape included.

Correcting the spectrum shown in figure 23 for this measured delay to the same trigger level as used in the photo diode measurement, a discrepancy between the calculated value t_c and $t_{m,\,corr}$ of (167 ± 122) ns is left. This includes the cooling time, uncertainties such as the initial distribution and temperature of the plasma and the uncertainties from the SIMION® model used to calculate the expected TOF. The signal propagation time difference of the laser trigger signal and the signal of the photo diode can be neglected

here since they are only in the order of a few ns. This leaves overall no big margin for cooling time assumptions, as the error is in the order of the measured delay. With expected cooling times of a few hundred ns, the left delay seems reasonable though. To allow more precise measurements, the resolution of the TOF spectra would have to be further increased.

Because of the limited resolving power achieved with such a short drift length and to be able to measure the produced ion current, the setup was modified. The drift length was increased to $(1.77 \pm 0.01)\,\mathrm{m}$ and a Faraday cup on a linear feedthrough was added to allow either a current measurement or a TOF analysis with the MCP. The target has been exchanged as well, now the second target as shown previously in figure 19 is used. The carbon plate was added in order to produce carbon clusters as observed in other experiments [46, 61]. The cluster ions, such as $^{12}\mathrm{C}_n^+$ with $n = 1, 2, 3 \ldots$, might be useful for a TOF calibration. The target exchange itself proved to be simple. To this end, the system was vented with nitrogen to keep lighter gasses out. The exchange takes about $30\,\mathrm{min}$ if the new target is already produced and ready to be attached. After changing the target, the source was ready for operation again within $12\,\mathrm{h}$, reaching a pressure of $1.4 \times 10^{-9}\,\mathrm{mbar}$. The pressure before the target change was only slightly lower at $6 \times 10^{-10}\,\mathrm{mbar}$ but increases to the low $10^{-9}\,\mathrm{mbar}$ range during operation anyway. Overall, about one day is required to exchange the target and have the LIS ready for operation again. Due to the now larger distance to the MCP, the extraction voltages have to be increased to keep the total expansion of the beam after leaving the last einzel lens similar to the previous run. Additionally, the voltage difference between the first and the second acceleration electrode has to be decreased to move the time focal point onto the new MCP plane. The first acceleration voltage is chosen to be $U_{\mathrm{Acc1}} = 2.3\,\mathrm{kV}$. Higher extraction potentials would require lens voltages exceeding the available $-6\,\mathrm{kV}$ to keep the beam spatially focused on the MCP. As this would force a switch to positive einzel lens voltages, the extraction voltage is not further increased for now.

To achieve a time focus on the MCP with the first acceleration voltage chosen, the second voltage can be calculated. It is found to be $U_{\mathrm{Acc2}} \approx 2.17\,\mathrm{kV}$. To further increase the beam quality, the difference between first and second electrode can be increased. This lowers the radial expansion due to lower accelerations times and reduces the turn-around time.

To do this without changing the time focus point, the third electrode is utilized. By increasing U_{Acc3}, the second electrode can be lowered while keeping the time focus on the same position. To find the possible combinations of U_{Acc2} and U_{Acc3} with the first electrode voltage fixed, SIMION® is used to minimize the temporal spread, as done for the previous determination of the required voltage (see figure 22). This yields multiple

similar possibilities from which $U_{\text{Acc2}} = 2040\,\text{V}$ and $U_{\text{Acc3}} = 560\,\text{V}$ are chosen for the initial setup. These are then further optimized by maximizing the measured current of the ion beam using the Faraday cup and the signal strength observed on the MCP, while keeping the signal width small. An optimum has been found for the voltages of $U_{\text{Acc2}} = 2\,\text{kV}$ and $U_{\text{Acc3}} = 650\,\text{V}$, achieving a compromise between extraction efficiency and time focus. These voltages are used in the following unless noted otherwise. The voltage settings for the three einzel lenses and steering electrodes can be used in many different combinations. In general, the einzel lenses are operated with negative voltages due to the lower aberration effects as shown in 12. Positive voltages have been tested as well but did not show any significant differences.

5.3 TOF measurements with the second configuration

For the measurement with the second target the pulse repetition rate is lowered to $10\,\text{Hz}$ with a pulse energy of $E_{\text{p}} = (2.33 \pm 0.04)\,\text{mJ}$. The measured spectra are corrected for the previously determined laser pulse offset. The calculated TOF is extracted from SIMION® with the uncertainty being the standard deviation of the TOF due to the ion starting distribution and the uncertainty of the drift length with $L_{\text{D}} = (1.77 \pm 0.01)\,\text{m}$. The result is shown in figure 25.

While all measured and calculated times are in agreement within their errors, the offset still left is now smaller compared to the previous measurement after the correction of the laser pulse delay. The measurement is performed on a ablation spot, that was being used for several minutes prior to the recording of the spectrum. Despite that, contamination is showing. The first one is identified as $^{12}C^{+}$ which is plausible since measurements with the carbon target have been performed prior to recording this spectrum. The ablated carbon seems to sputter onto the surfaces and shows up for several minutes but is observed to become smaller for longer measurement times. For new ablation spots the peak is strongest, validating the assumption of surface contamination.

The double peak in the aluminum-beryllium spectrum, labeled as *cluster ions*, is assigned to $AlBe_2^{+}$ and $^{27}Al_2^{+}$ clusters. For the $^{27}Al_2^{+}$ a TOF of $t_c = (19.64 \pm 0.15)\,\mu\text{s}$ is calculated, while the measurement shows a peak at $t_{\text{m}} \approx 19.5\,\mu\text{s}$, thus is in excellent agreement.

Directly after the measurement of the spectrum, an ion beam current measurement is performed by using the Faraday cup. No parameters of the setup have been changed for that. The ion current for the aluminum-beryllium spectrum is measured as an average of 10 individual measurements, each $5\,\text{s}$ long. Therefore, the total measurement averages over a total of 500 pulses. This results in $I_{\text{total}} = (97.6 \pm 2.4)\,\text{pA}$, measured with the repeller electrode of the Faraday cup set to $U_{\text{repel}} = -500\,\text{V}$. This value is found by

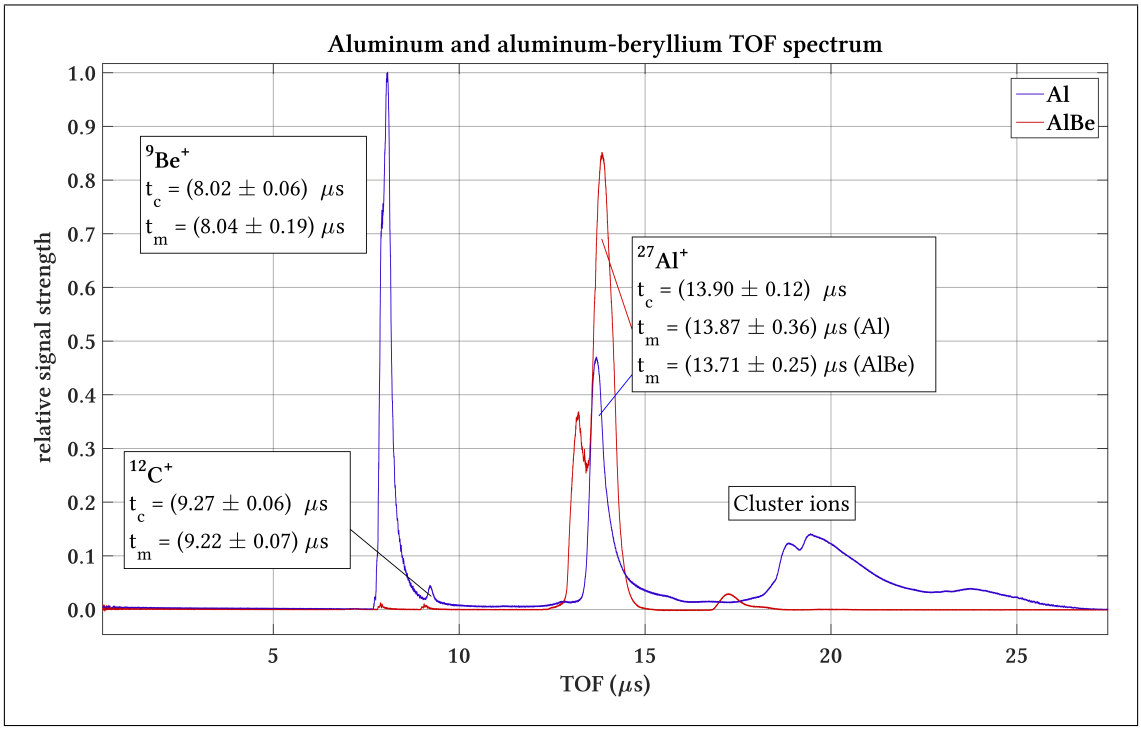

Figure 25: The TOF spectrum of aluminum-beryllium (blue) and aluminum (red) averaged from 256 single shot spectra is shown. The signals are scaled relative to the beryllium peak. For details see text.

increasing the voltage until the current is no longer going down, then increasing it by an additional 80 V to assert that no secondary electrons will leave the cup. This actually increases the current again slightly ($\approx 1\,\mathrm{pA}$ on average), probably due to the negative voltage "pulling" additional ions into the cup which otherwise would not hit the Faraday cup opening of only $\approx 16\,\mathrm{mm}$.

The measured current is assumed to result solely from singly charged ions, as no $^{9}Be^{2+}$ or $^{27}Al^{2+}$ are observed in the previous measurements. Lacking means of separation of the different ion species in the offline setup, the measured current is the total beam current of all ions. The total ion count per pulse N_P can be calculated as

$$N_P = \frac{I_{total}}{q f_{laser}} = (6.1 \pm 0.1) \times 10^7 \tag{5.1}$$

with $q = e$, and the pulse repetition rate $f_\mathrm{laser} = 10\,\mathrm{Hz}$. This is already in the range, where a beginning saturation of the MCP can be expected [48].

To estimate the amount of beryllium ions, the areas of the TOF signals observed on the MCP are used. For this, a measurement with the same laser intensity is used to produce the same ratio of ions. To reduce the total number of ions hitting the MCP, the beam is defocused though. This assures that the measurement is performed in the linear range

of the MCP response. The current is lowered to an average of $I_c = (6.5 \pm 1.2)\,\mathrm{pA}$ by this. This corresponds to a total ion count per pulse of $N_P = (4.1 \pm 0.7) \times 10^6$. From the measurement performed with this follows, that about 42% of the total current results from $^9Be^+$ ions. Performing the same evaluation with the beam focused on the MCP results in about 53% for the beryllium ion percentage. Here, the percentage of 42% is used for further evaluation to provide a lower limit estimation. The optimized current of $I_{\mathrm{total}} = (97.6 \pm 2.4)\,\mathrm{pA}$ corresponds to about 2.6×10^7 $^9Be^+$ ions per pulse arriving at the Faraday cup.

With the estimated number of some 10^6 beryllium ions required in the trap, this means a trapping efficiency of about 4% has to be achieved. To estimate the transfer efficiency, the following points have to be taken into account: With a beam diameter of about $8\,\mathrm{mm}$ when leaving the extraction unit, the first big limitation will be the quadrupole benders in the beamline. Another big fraction is expected to be lost upon entering the drift tube, as the lowered energy causes the beam to expand and hit the tube. Finally, a last einzel lens is used to focus the ions into a CF16 tube with a length of about $1.2\,\mathrm{m}$ upon leaving the drift tube. At the end of this tube, the ions reach the cryostat and the magnetic field will help to guide the ions towards the trap. A SIMION® simulation for the benders, drift tube and this CF16 tube and a three sets of einzel lenses distributed in the beamline is performed as an estimation of the achievable transfer efficiency. The starting parameters of the ion distribution are the same as previously used (see section 3.6). The simulation predicts about 9% of the produced ions to reach the end of the CF16 tube after being pulsed down by the drift tube to an energy of E $\approx 800\,\mathrm{eV}$. This simulated efficiency was achieved without a complete sweep of the possible parameters, therefore the voltages of the quadrupole bender and the numerous einzel lenses are not expected to be fully optimized yet. The simulation should still only be taken as an order-of-magnitude estimation due to the large variety of parameters. The schematic shown in figure 26 gives an overview of the included elements and distances of this simulation. The drift tube is on a potential of $U_{\mathrm{drift}} = 1500\,\mathrm{V}$ and set to $U_{\mathrm{drift}} = 0\,\mathrm{V}$ when the ions are about $10\,\mathrm{cm}$ inside.

The quadrupole benders keep the beam in the same plane in the simulation as opposed to the actual setup. Only about 30% of the ions are expected to pass the quadrupole benders, as extracted from the simulation. With the total amount of ions transported to the magnet already being on the same order of the ions required, a successful trapping can presumably be achieved.

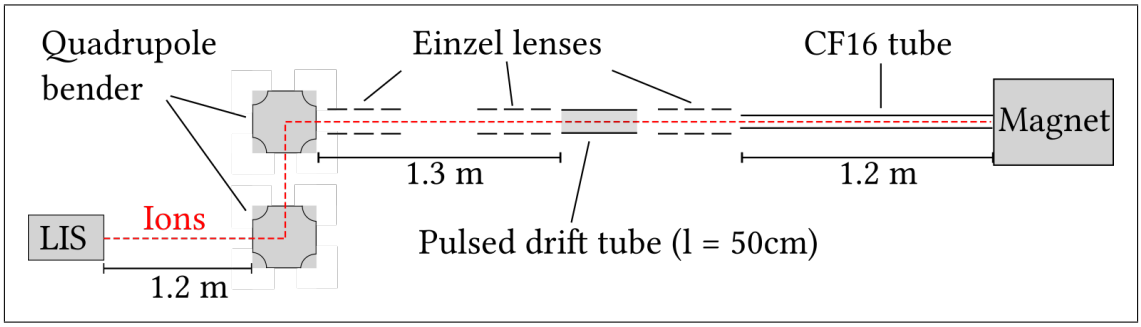

Figure 26: A schematic of the simulated transfer path with the included ion optics. The distances are not to scale. For details see text.

5.4 Evaluation of the ion beam current

As a measurement in the pA range is prone to errors due to systematic offsets, multiple tests were performed to make sure that the measured current corresponds to only the ions and no other signals. Such an evaluation is shown in figure 27.

The noise measurements I_{D0} to I_{D4} have been performed for different settings for which no ions are expected to arrive at the Faraday cup. To measure I_{D0} the laser is running, but the laser shutter is closed. All electrical signals are therefore the same but the laser never passes into the setup. For I_{D1}, the third acceleration electrode is set to $U_{\mathrm{Acc3}} = 4\,\mathrm{kV}$. With $U_{\mathrm{Acc1}} = 2.3\,\mathrm{kV}$ and $U_{\mathrm{Acc2}} = 2\,\mathrm{kV}$ being significantly lower, the produced ions are reflected back onto the target and cannot leave the acceleration stage.

I_{D2} is measured with all acceleration electrodes being set to $0\,\mathrm{V}$. The ions are produced but not accelerated towards the Faraday cup. Finally, for the I_{D3} measurement the Faraday cup is simply removed from the beam path, with the ions now hitting the MCP again. This has been assured by the observed signal on the phosphor screen. All current measurements, I_1, I_2 and I_3 are performed with the standard settings, with the total beam current being slightly lower compared to the previous measurement (see section 5.3) due to a lower laser pulse energy of $E_p = (1.54 \pm 0.03)\,\mathrm{mJ}$.

While the first three noise measurements are in agreement, I_{D3} with the cup removed from the beam shows a negative current. This is thought to be due to secondary electrons being produced when the ions hit the drift tube or a sputter on the einzel lenses. The dark current of $I_{\mathrm{D}} = (0.27 \pm 0.08)\,\mathrm{pA}$ from the first three measurements is used to correct the measurements discussed in the following. The current measurement of I_1 to I_3 is slightly decreasing. This is due to the ablation spot being unchanged for this measurement campaign, which took about $15\,\mathrm{min}$, resulting in a decreasing ion yield.

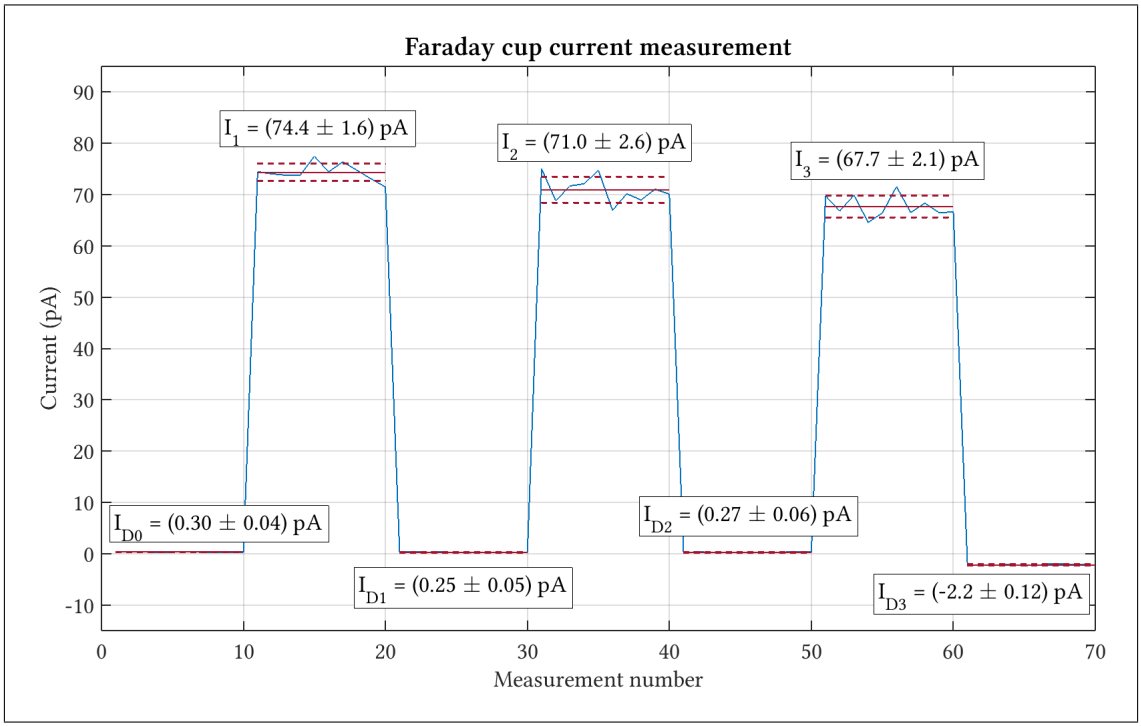

Figure 27: A current measurement with the Faraday cup. The ion beam is blocked in multiple ways to compare the noise measurements I_{D0} to I_{D4}. The actual ion beam current measurements I_1 to I_3 are all performed with the same settings, the slowly decreasing current is due to the continuous use of the same ablation spot for about $15\,\mathrm{min}$ ($\approx$ 9000 shots).

5.5 Laser settings

To characterize the dependance of the laser settings, namely the pulse energy, spectra for different settings were recorded. Additionally, the current has been measured as well. The result is shown in figure 28.

The measurement starts with the lowest pulse energy of $E_p = (1.29 \pm 0.03)\,\mathrm{mJ}$ at which $^9\mathrm{Be}^+$ ions could be observed. This already gives a well observable signal for aluminum ions with a slightly deformed peak. Interestingly, this produces the largest signals for cluster ions such as $^{27}\mathrm{Al}_2^+$, $^{27}\mathrm{Al}^9\mathrm{Be}^+$ or $^{27}\mathrm{Al}^9\mathrm{Be}_2^+$, with weak signals for all other species. Due to the lower power density, the ablation and plasma ignition might leave more clusters than single atoms, resulting in more ionized clusters than single ions. The total current is $I_{\mathrm{total}} = (22.6 \pm 1.9)\,\mathrm{pA}$

Increasing the laser pulse energy to $E_{\mathrm{p}} = (1.54 \pm 0.03)\,\mathrm{mJ}$ results in a nicely shaped beryllium peak with the aluminum peak still being more pronounced though. The ratio of beryllium to aluminum ions is increased by roughly a factor 4 in this measurement. The intensities for the cluster ions are slightly decreasing compared to the lower energy

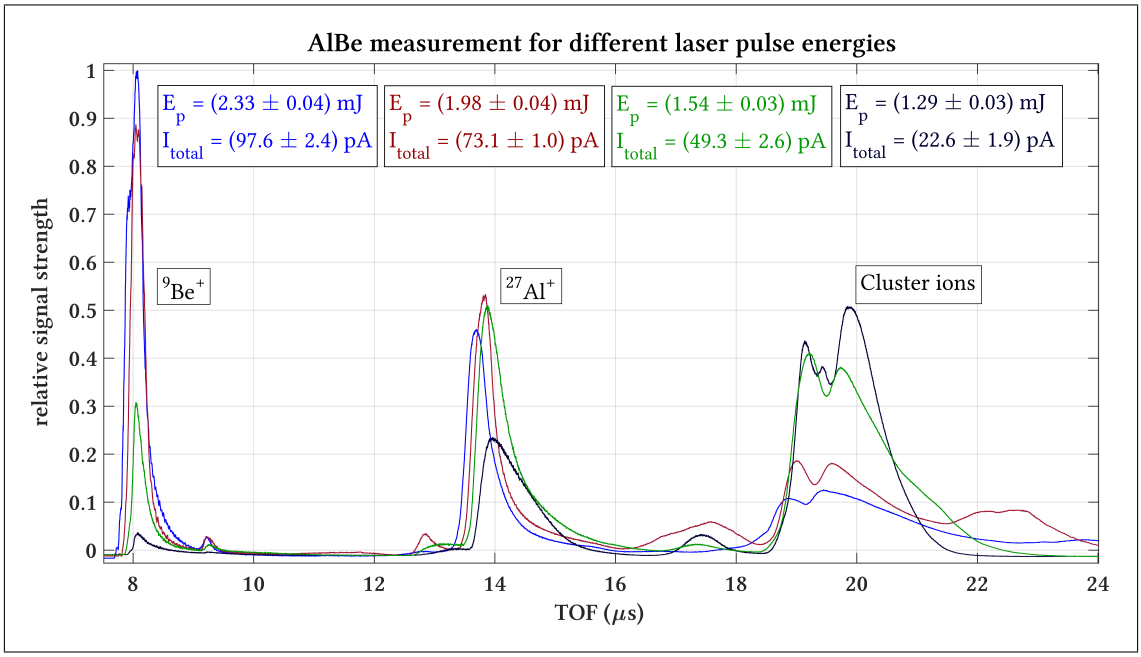

Figure 28: The dependance of the laser pulse energy on the ion yield is shown. The first measurement (black) corresponds to the lowest energy setting with which beryllium ions could be observed. The highest energy matches the previously shown spectra. The signals are scaled relative to the maximum of the beryllium ion signal at the highest measured energy (blue).

measurement. The total current is more than doubled, resulting in $I_{\text{total}} = 49.3\,\text{pA}$.

With an energy of $E_{\text{p}} = (1.98 \pm 0.04)\,\text{mJ}$, the current is again increased by roughly 50% compared to the previous measurement while the yield for cluster ions now drops significantly. The intensity of the observed beryllium peak is almost tripled now, while the aluminum intensity stays nearly the same. This might be explained by the power density being already sufficient to ionize the aluminum with good efficiency whereas the beryllium requires a higher power density for ions to be produced in good quantities. From the lowered cluster ion yield one might also conclude, that the beryllium is no longer mainly ablated in clusters but is now produced as single atoms.

Finally, the measurement with a laser pulse energy of $E_{\text{p}} = (2.33 \pm 0.04)\,\text{mJ}$ shows only a slight increase in the intensity of the beryllium peak compared to the previous measurement. It should be noted that the peak starts to deform on the left side, which might indicate a beginning saturation of the MCP. While the total current again increases, the yield of aluminum ions and cluster ions goes down. As the intensity of the beryllium peak is not increasing significantly though, the maximum efficiency seems to be reached. Increasing the power even further produced a highly deformed beryllium peak due to a definite saturation, while first doubly charged ions could be observed. Since this

complicates current measurements and because the production of higher charged ions is not the aim of this source, this is not further evaluated at this point.

5.6 Pressure measurement

The pressure was monitored over the course of the previous measurement, showing an increase from $p_0 = 6 \times 10^{-10}\,\mathrm{mbar}$ before the laser is switched on to about $p_\mathrm{f} = 2.5 \times 10^{-9}\,\mathrm{mbar}$ at the end of the measurement series. After switching the laser off, it takes about $1.5\,\mathrm{h}$ to reach the previous level again. This is about a factor of 50 higher compared to the pressure in the connected beamline. The LIS will be connected to this by a CF40 tube with a length of $l \approx 20\,\mathrm{cm}$, including a valve. The molecular flow conductivity C_total of air at a temperature of $293\,\mathrm{K}$ through a short tube can be estimated [62] as

$$\frac{1}{C_\mathrm{total}} \approx \frac{1}{C_\mathrm{aperture}} + \frac{1}{C_\mathrm{tube}} \tag{5.2}$$

$$\approx \frac{1}{11.6A} + \frac{l}{12.1d^3} \tag{5.3}$$

with the aperture of the pipe A in cm^2, the diameter d and length l of the tube in cm.

This yields approximately $C_\mathrm{total} \approx 30\,\frac{\mathrm{L}}{\mathrm{s}}$. With the pressures during the operation of the LIS $p_\mathrm{LIS} \approx 2.5 \times 10^{-9}\,\mathrm{mbar}$ and in the section of the quadrupole benders $p_\mathrm{bender} \approx 6 \times 10^{-11}\,\mathrm{mbar}$, the required pumping speed S in the bender section to sustain that pressure difference can be estimated [63] as

$$S \approx \left(\frac{p_\mathrm{LIS}}{p_\mathrm{bender}} - 1\right) \cdot C_\mathrm{total} \tag{5.4}$$

$$\approx 1200\,\frac{\mathrm{L}}{\mathrm{s}} \quad . \tag{5.5}$$

With a directly connected pump featuring a pumping speed of $800\,\frac{\mathrm{L}}{\mathrm{s}}$, a second pump of the same type close by, and a not yet used getter pump [64] featuring a pumping speed of $410\,\frac{\mathrm{L}}{\mathrm{s}}$, the pressure seems to be sustainable. The pressure p_bender can definitely be expected to increase less than one order of magnitude.

5.7 Carbon target measurements

Since the carbon target is expected to produce cluster ions with different numbers of carbon atoms, the TOF spectrum should be easy to calibrate. The spectrum is measured with a pulse energy of $E_p = (1.54 \pm 0.03)\,\mathrm{mJ}$. For the calibration, the simple case

of ions with a constant energy – neglecting acceleration and effects by the lenses – is assumed. The TOF t_c can then be written as

$$t_c = \underbrace{\left(\frac{x_\mathrm{d}}{\sqrt{2E_\mathrm{ion}}} \right)}_{A} \cdot \sqrt{m_\mathrm{ion}} + t_0 \tag{5.6}$$

with the drift length to the MCP x_d, the total kinetic energy E_ion, the ion mass m_ion and an offset time t_0. A function of this form is fitted to the measured arrival times of the carbon ions. The peaks are identified by comparing the TOF calculated by SIMION® with the measured data. For the fit the carbon clusters $^{12}\mathrm{C}_n^+$ with $n = 1$ to 12 are used. This results in the parameters $A_\mathrm{fit} = (2.722 \pm 0.008) \times 10^{-6}\,\mathrm{s}/\sqrt{\mathrm{u}}$ and $t_0 = (193 \pm 72)\,\mathrm{ns}$.

Calculating A with the known values of $x_\mathrm{d} = (1.77 \pm 0.01)\,\mathrm{m}$ and $E_\mathrm{ion} \approx 2.3\,\mathrm{keV}$ results in $A_\mathrm{calc} = (2.657 \pm 0.017) \times 10^{-6}\,\mathrm{s}/\sqrt{\mathrm{u}}$. The fitted value of A is slightly larger than the simplified theoretical model since the acceleration time scales $\propto \sqrt{m_\mathrm{ion}}$ as well, adding to the result and increasing the value.

The offset t_0, here fitted without correcting for the laser offset, is found to be $t_0 = (193 \pm 72)\,\mathrm{ns}$. This is smaller than the extracted offset from the laser delay. This can be explained by the measurement of the spectrum being performed with all einzel lenses on negative potentials ($U_\mathrm{L1} = -2.8\,\mathrm{kV}$, $U_\mathrm{L2} = -4.05\,\mathrm{kV}$, $U_\mathrm{L3} = -2.75\,\mathrm{kV}$), momentarily increasing the energy and lowering the TOF. Additionally, the front-plate of the MCP is set to $U_\mathrm{MCP} = -1.6\,\mathrm{kV}$ also increasing the energy and therefore lowering the measured TOF. In SIMION® both effects can be evaluated as the difference between the TOF with the lenses and the MCP set to their respective potentials and the TOF with all of them grounded. For $^{12}\mathrm{C}^+$ this corresponds to a difference in the TOF of $\Delta t_\mathrm{c} = (291 \pm 54)\,\mathrm{ns}$. This results in the ions arriving earlier than predicted by the fit model, lowering the offset of the fitted function. The resulting spectrum is shown in figure 29.

The calibrated spectrum shows a very good agreement for all carbon cluster peaks. Additionally, a peak at mass $m = (39.73 \pm 0.92)\,\mathrm{u}$ is observed which probably corresponds to potassium $^{39}\mathrm{K}^+$ from surface contamination or an abundance in the target material due to the production. As the current is very low compared to the measurements performed with the aluminum-beryllium target with similar pulse energies and the high cluster yield of at least up to $^{12}\mathrm{C}_{15}^+$, a similar laser pulse energy measurement is performed. The intensities are scaled relative to the maximum of the measurement shown in figure 29 to allow a direct comparison. To perform a mass calibration the parameters extracted from the previous fit are used. This can be used to assure that the fitting parameters stay similar, at least for the same target. The measurement is shown in figure 30.

The increased pulse energy of $E_\mathrm{p} = (1.76 \pm 0.03)\,\mathrm{mJ}$ directly results in the current

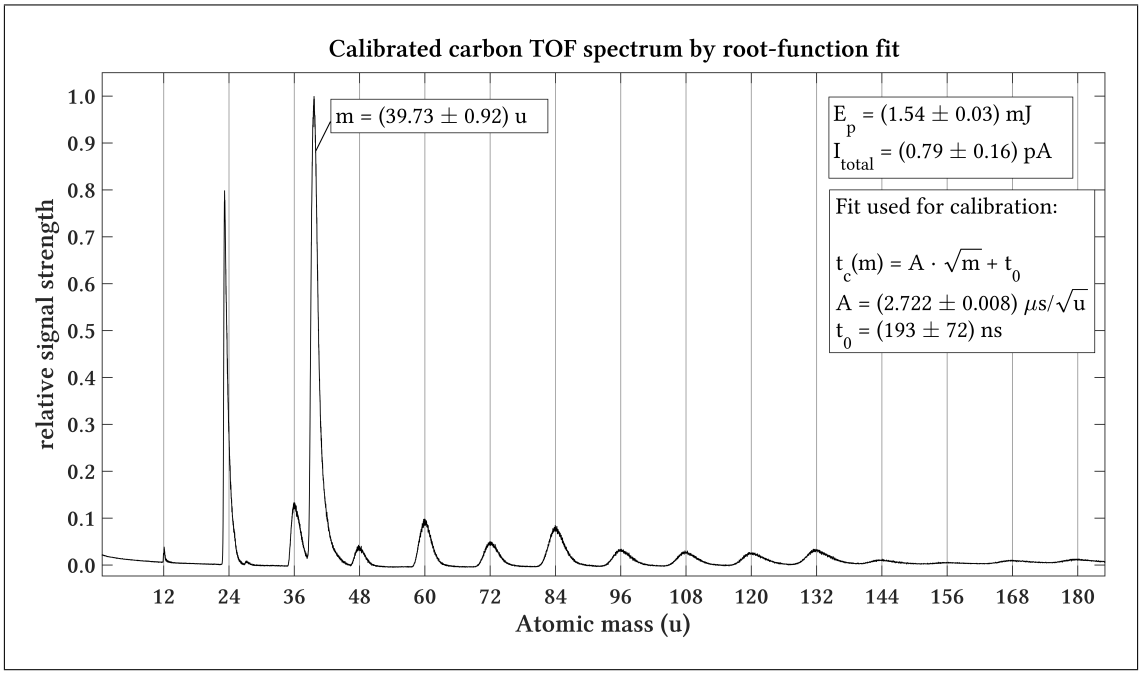

Figure 29: Measurement of mass spectrum using a carbon current. The calibration was done by fitting a root-function with offset to the measured data. For details see text.

increasing by more than a factor of 4. The yield of single carbon ions is greatly increased, though the $^{12}C_2^+$ cluster ions show the highest intensity about 7 times higher than before whereas in the previous measurement the potassium contamination was strongest. This stays on about the same level as before, around an intensity of 1. The overall spectrum is now more pronounced towards the lighter masses, all showing an increased intensity. Using even more energy, with $E_\mathrm{p} = (1.96 \pm 0.03)\,\mathrm{mJ}$, this effect is even stronger pronounced. The single carbon ions now show similar intensities compared to the $^{12}C_2^+$ cluster ions, with the total current increasing again by more than a factor of 4. While the intensities of the cluster ions stay very similar, the shape of the peaks starts to widen. This might be explained by either an increased kinetic energy spread due to higher temperatures or an increasing cooling time spread of the ions. Since the achieved resolution is rather low for higher masses, the effect cannot be evaluated in depth here. The change of the production efficiency from multiple atom cluster ions yield towards single ions by increasing the pulse energy as observed is similar for the aluminum-beryllium target but significantly stronger pronounced here. It should be noted though, that the total ion current is significantly lower compared to the metal targets with the same pulse energy used. The calibration used from the previous measurement fits the data nicely, as all peaks are still on point. In a different measurement when the

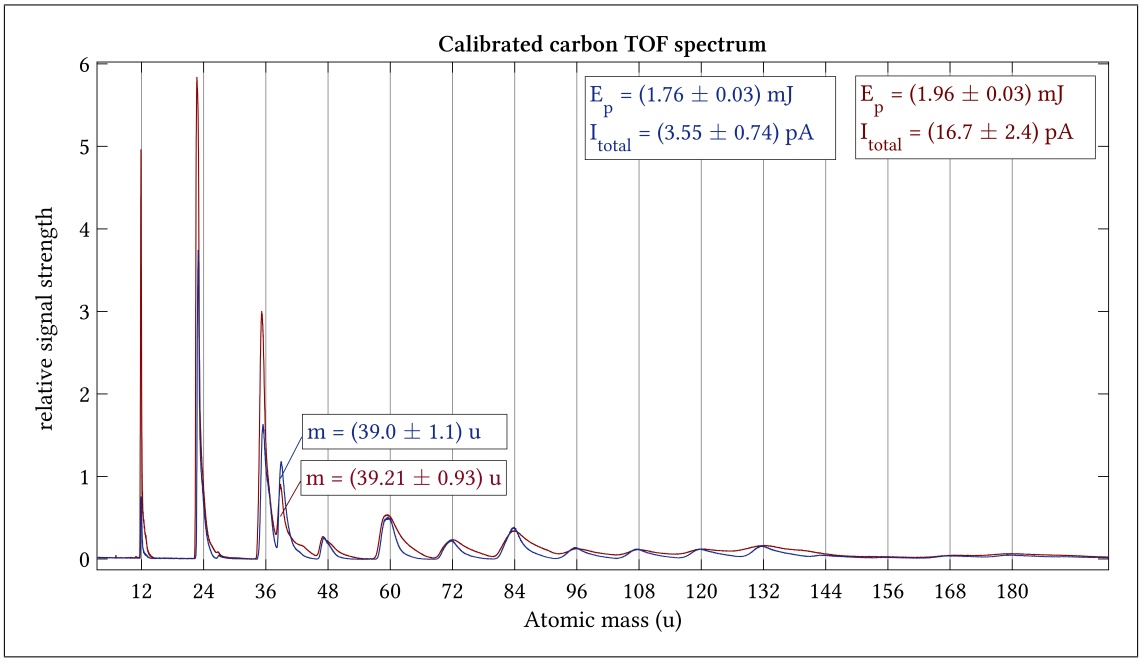

Figure 30: The measurement shows two different settings of the laser pulse energy, both are scaled to compare to the previous measurement. The blue curve, with a pulse energy of $E_\mathrm{p} = (1.76 \pm 0.03)\,\mathrm{mJ}$ shows a shift of the ion yield towards smaller clusters. The $^{12}C_2^+$ now has the highest intensity, while the contamination of $^{39}K^+$ stays on the same intensity as in the previous measurement, where it was used as reference intensity 1. The red curve shows a higher pulse energy of $E_\mathrm{p} = (1.96 \pm 0.03)\,\mathrm{mJ}$, highly increasing the $^{12}C^+$ yield, with the potassium still at about the same level.

pulse energy was increased even further, $^{12}C^+$ showed the strongest signal, following the same trend that can be observed here.

6 Conclusion and outlook

To recapitulate, implementing sympathetic laser cooling in the ALPHATRAP experiment requires $^9Be^+$ ions. Depending on the chosen approach, either a single or up to about 10^6 ions will have to be trapped to achieve this. The ions need to be transported over a distance of about $4.5\,\mathrm{m}$ from the LIS to the trap through a beamline and arrive focused in time and space to provide means of ion species selection and achieve an efficient trapping. The source has to be directly attached to the beamline, requiring a similar vacuum of about $6 \times 10^{-11}\,\mathrm{mbar}$.

The three-stage acceleration was shown to achieve the required time-focus as can be concluded from the well-resolved signals of the MCP. The simulation of the extraction process has shown that the main contaminant of aluminum ions is still well separated from the beryllium ions after they enter the drift-tube. As the simulated values for the TOF are in agreement with all measurements, an ion selective operation of the pulsed-drift-tube is expected.

Varying the laser intensity showed a definite tendency towards smaller cluster and single ions with increasing energies. This was clearly observed in the carbon measurements and has also been seen in the spectra of the aluminum-beryllium target.

The energy dependance showed a clear tendency towards smaller clusters with increasing energies. This could be observed very clearly in the carbon measurements and the insights gained here seem to be applicable to the measurements with the aluminum-beryllium target as well. The measured carbon spectra allowed the fitting of the expected TOF and showed well agreements with the expected values.

The LIS is proven to consistently produce the required beryllium ions without the need of permanent maintenance. This can be concluded from the extensive measurements of the aluminum-beryllium target over the course of two months, which were be performed on a daily basis without problematic behavior or the need for target exchanges. A big advantage of a LIS observed here is that ions can be produced within a few minutes of notice with consistent results if the vacuum is sustained.

The estimated ion current of about 2.6×10^7 beryllium ions per laser pulse is assumed to provide sufficient ions arriving at the trap, as a SIMION® simulation shows about 9% of the ions reaching the end of the CF16 tube where the magnetic field starts to guide the ions. With their energy already being lowered to about $800\,\mathrm{eV}$, they are expected the be trappable. A final demonstration of trapping $^9Be^+$ ions is yet to be done though.

It was possible to produce ions from different materials, including copper, aluminum, carbon and obviously beryllium, showing the versatility of the ion source.

A pressure of $6 \times 10^{-10}\,\mathrm{mbar}$ is achieved when the source is not operated – even

with the glued target. While ions are produced, the pressure is increased to about $2.5 \times 10^{-9}\,\mathrm{mbar}$. As the estimation of the differential pumping shows, the pressure difference compared to the beamline vacuum of about 6×10^{-11} should be sustainable. If no ions are produced, the connection valve can be closed to achieve a vacuum similar as without an attached source.

Concluding this thesis, a laser ion source was designed, built and successfully tested in an offline setup. The detailed tests yielded promising results, beginning with the consistent functionality, providing high quantities of $^9Be^+$ ions and showing well-separated ion signals from other species present in the spectra. Subsequently, the LIS is fulfilling the required conditions.

With a reliably working ion source, the next step is to move and attach the LIS to the beamline, where further testing of the ion transport will be performed. Additional measurements, such as a characterization of the energy spread of the ions might be required. In the currently used model, a difference of up to $\Delta E_{\mathrm{kin}} = 75\,\mathrm{eV}$ solely due to different starting positions is included. This directly translates to the maximum energy of the ions when they are trapped. If the ions can be cooled with these large energies remains to be tested. If the measured energy spread turns out to be lower than presently assumed, the simulated transfer efficiency would increase. Further optimizations of the extraction and lens voltages to match the conditions of the beamline might additionally increase this efficiency.

To improve the yield of $^9Be^+$ ions, several different approaches can be investigated. Foremost, the maximum laser pulse energy used so far was only $E_{\mathrm{p}} = (2.33 \pm 0.04)\,\mathrm{mJ}$ of the available $35\,\mathrm{mJ}$. This was mainly due to beginning saturation effects of the MCP and to keep the pressure as low as possible. Increasing the pulse energy while slightly defocusing the laser beam would result in the same power density used so far but with a larger ablation area. It seems likely, that this would result in a higher ion yield.

It would also be possible to simply increase the transfer energy of the ions from the LIS, lowering the spread of the ion beam. This would presumably result in an increased transfer efficiency up to the pulsed drift tube and will be tested as soon as the source is attached to the beamline.

As the ablation laser can be used with different wavelengths, this might hold additional possibilities to increase the ion yield. To ionize beryllium, the required photo-ionization energy corresponds to a wavelength of $133\,\mathrm{nm}$. With another frequency doubling of the laser, a wavelength of $266\,\mathrm{nm}$ can be produced. A then possible two-photon ionization process could lead to a higher number of $^9Be^+$ ions. This would be possible, if the ablation process is faster then the laser pulse length of $(7.9 \pm 0.2)\,\mathrm{ns}$ to produce free beryllium atoms, which then would be ionized. As different wavelengths require only the optical

setup to be modified, this is planned to be tested soon.

Additionally, the required ions do not have to be trapped in a single process. Multiple ion bunches can be stacked in the trap as has been shown at ISOLTRAP [65] for example. If one considers only a certain percentage of the already trapped ions to be lost each time the potential is pulsed down to capture another bunch of ions, the total number of stored ions can be increased by multiple capture processes. The total amount of ions that can be captured obviously depends strongly on the loss rate and how well it can be optimized.

As in the current simulation model a percentage of about 70% of the ions are expected to hit the quadrupole bender electrodes, an aperture might have to be implemented to lower the beam diameter and prevent that. An additional einzel lens closer to the quadrupole benders could be installed in the second cross of the vacuum chamber as well, lowering the amount of ions hitting the bender electrodes while increasing the transfer efficiency.

The injection of externally produced ions into the ALPHATRAP experiment is the next major step to be taken for the whole experiment. This is scheduled as the priority for the upcoming months, where it would be advantageous to have two independent ion sources (the table-top EBIT and the LIS) available to optimize the ion transfer. This would be a major step for the purpose of the LIS as well, since as soon as the injection and successful trapping is achieved, the implementation of laser cooling in the trap can be further developed. The cooling laser is currently being prepared for the access into the trap as the topic of the PhD thesis of Alexander Egl and will presumably be ready for first test runs in the near future.

Finally, an CAD simulation of the beamline setup shows the planned position of the LIS connected to the beamline in figure 31.

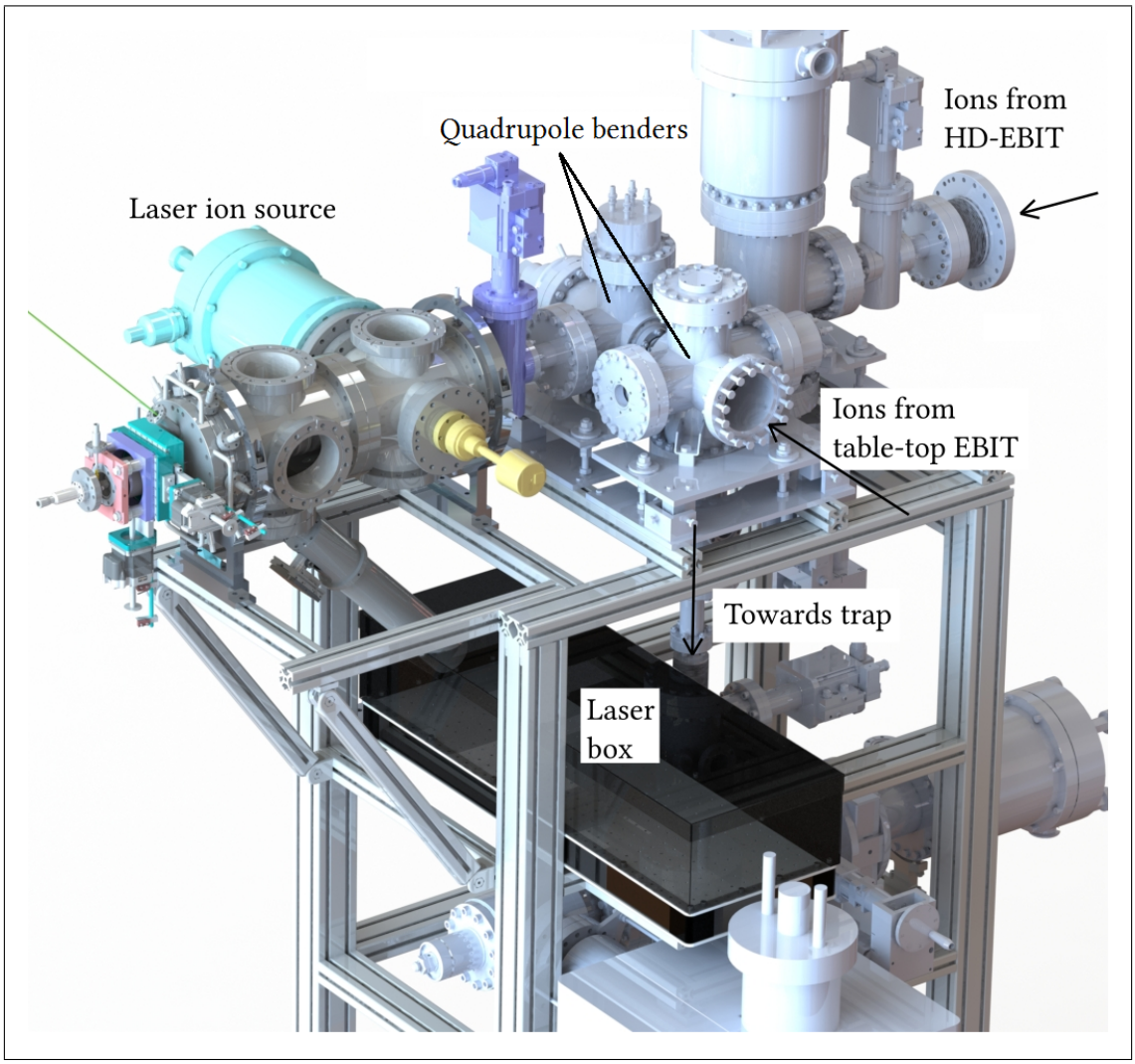

Figure 31: The model shows how the LIS is to be implemented into the existing beamline.

References

[1] D. Hanneke, S. Fogwell, and G. Gabrielse, "New measurement of the electron magnetic moment and the fine structure constant", Physical Review Letters **100**, 1–4 (2008).

[2] S. Sturm et al., "High-precision measurement of the atomic mass of the electron", Nature **506**, 467–470 (2014).

[3] S. Sturm et al., "g factor of hydrogenlike $^{28}Si^{13+}$", Physical Review Letters **107**, 023002 (2011).

[4] H. Häffner et al., "High-accuracy measurement of the magnetic moment anomaly of the electron bound in hydrogenlike carbon", Physical Review Letters **85**, 5308–5311 (2000).

[5] A. Wagner et al., "g factor of lithiumlike silicon $^{28}Si^{11+}$", Physical Review Letters **110**, 023002 (2013).

[6] J. R. C. López-Urrutia et al., "Optimization of the charge state distribution of the ion beam extracted from an EBIT by dielectronic recombination", Review of Scientific Instruments **75**, 1560–1562 (2004).

[7] B. D'Urso, B. Odom, and G. Gabrielse, "Feedback Cooling of a One-Electron Oscillator", Physical Review Letters **90**, 043001 (2003), https://link.aps.org/doi/10.1103/PhysRevLett.90.043001.

[8] S. Sturm et al., "High-precision measurement of the atomic mass of the electron", Nature **506**, 467–470 (2014).

[9] S. Kraemer, "Towards Laser Cooling of Beryllium Ions at the ALPHATRAP Experiment", Master thesis (Universität Heidelberg, 2017).

[10] Nobelprize.org, *The nobel prize in physics 1965*, June 2017, http://www.nobelprize.org/nobel_prizes/physics/laureates/1965/index.html.

[11] H. Bethe, "The electromagnetic shift of energy levels", Physical Review **73**, 617–626 (1948).

[12] W. E. Lamb and R. C. Retherford, "Fine structure of the hydrogen atom by a microwave method", Physical Review **72**, 241–243 (1947).

[13] W. Gerlach and O. Stern, "Der experimentelle Nachweis der Richtungsquantelung im Magnetfeld", Zeitschrift für Physik **9**, 349–352 (1922).

[14] P. A. M. Dirac, "The Quantum Theory of the Electron", Proceedings of the Royal Society of London **117**, 610–624 (1928).

[15] J. Schwinger, "On quantum-electrodynamics and the magnetic moment of the electron [9]", Physical Review **73**, 416–417 (1948).

[16] G. Breit, "The Magnetic Moment of the Electron", Nature **122**, 649 (1928).

[17] V. M. Shabaev et al., "G-factor of heavy ions: A new access to the fine structure constant", Physical Review Letters **96**, 5–8 (2006).

[18] Z. Harman, *Private communications*, 2016.

[19] L. S. Brown and G. Gabrielse, "Geonium theory: Physics of a single electron or ion in a Penning trap", Reviews of Modern Physics **58**, 233–311 (1986).

[20] K. Blaum, Y. N. Novikov, and G. Werth, "Penning traps as a versatile tool for precise experiments in fundamental physics", Contemporary Physics **51**, 149–175 (2009).

[21] K. Blaum, "High-accuracy mass spectrometry with stored ions", Physics Reports **425**, 1–78 (2006).

[22] J. Ketter, "Verbesserungen der Ionennachweissysteme des Präzisions-Penningfallen-Massenspektrometers TRIGA-TRAP", Diploma Thesis (Johannes Gutenberg-Universität Mainz, 2009).

[23] S. Sturm, "The g-factor of the electron bound in $^{28}Si^{13+}$: The most stringent test of bound-state quantum", Dissertation (Johannes Gutenberg-Universität Mainz, 2012).

[24] A. Weigel, "Entwicklung des kryogenen Nachweissystems für ALPHATRAP und THe-Trap", Master thesis (Universität Heidelberg, 2014).

[25] H. Dehmelt, "Continuous Stern-Gerlach effect: Principle and idealized apparatus.", Proceedings of the National Academy of Sciences of the United States of America **83**, 2291–2294 (1986).

[26] S. Sturm et al., "Phase-sensitive cyclotron frequency measurements at ultralow energies", Physical Review Letters **107**, 143003 (2011).

[27] J. Ketter et al., "First-order perturbative calculation of the frequency-shifts caused by static cylindrically-symmetric electric and magnetic imperfections of a Penning trap", International Journal of Mass Spectrometry **358**, 1–16 (2014).

[28] G. Gabrielse, L. Haarsma, and S. L. Rolston, "Open-endcap Penning traps for high precision experiments", International Journal of Mass Spectrometry and Ion Processes **88**, 319–332 (1989).

[29] F. Köhler et al., "The electron mass from g-factor measurements on hydrogen-like carbon $^{12}C^{5+}$", (2016) 10.1088/0953-4075/48/14/144032.

[30] D. J. Larson et al., "Sympathetic cooling of trapped ions: A laser-cooled two-species nonneutral ion plasma", Physical Review Letters **57**, 70–73 (1986).

[31] V. S. Letokhov and V. G. Minogin, "Cooling, trapping, and storage of atoms by resonant laser fields", Journal of the Optical Society of America **69**, 413 (1977).

[32] A. Ashkin, "Motion of atoms in a radiation trap", Physical Review A (General Physics) **21**, 1606–1617 (1980).

[33] P. D. Lett et al., "Optical molasses", Journal of the Optical Society of America B **6**, 2084 (1989).

[34] V. A. Yerokhin et al., "g-Factor of Light Ions for an Improved Determination of the Fine-Structure Constant", Physical Review Letters **116**, 1–5 (2016).

[35] S. Sturm, *Private communications*, June 2017.

[36] H. Hirzler, "Aufbau und Test der Transferbeamline für das ALPHATRAP Projekt", Bachelor thesis (Universität Heidelberg, 2014).

[37] A. Egl, "Commissioning of the offline transfer beamline for the ALPHATRAP experiment", Master thesis (Universität Heidelberg, 2016).

[38] R. Jordan et al., "Pulsed laser ablation of copper", Applied Surface Science **86**, 24–28 (1995).

[39] I. Brown, *The physics and technology of ion sources* (Wiley-VCH, Weinheim, 2004).

[40] M. Capitelli et al., "Laser-induced plasma expansion: Theoretical and experimental aspects", Spectrochimica Acta - Part B Atomic Spectroscopy **59**, 271–289 (2004).

[41] B. Sharkov and R. Scrivens, "Laser Ion Sources", **33**, 1778–1785 (2005).

[42] J. G. Lunney and R. Jordan, "Pulsed laser ablation of metals", Applied Surface Science **127**, 941–946 (1998).

[43] B. K. Mann and K. Rohr, "Differential measurement of the absolute ion yield from laser-produced C plasmas", Laser and Particle Beams **10**, 435–446 (1992).

[44] U. Rohner, J. A. Whitby, and P. Wurz, "A miniature laser ablation time-of-flight mass spectrometer for in situ planetary exploration", Measurement Science and Technology **14**, 2159–2164 (2003).

[45] K. Blaum et al., "Cluster calibration in mass spectrometry: Laser desorption/ionization studies of atomic clusters and an application in precision mass spectrometry", Analytical and Bioanalytical Chemistry **377**, 1133–1139 (2003).

[46] C. Smorra et al., "A carbon-cluster laser ion source for TRIGA-TRAP", Journal of Physics B: Atomic, Molecular and Optical Physics **42**, 154028 (2009).

[47] Litron, *Litron Nano s Datasheet*, http://www.litronlasers.com/pdf%20files/Nano%20Range%20Spec%20PB0108_1.pdf (visited on 05/08/2017).

[48] J. Ladislas Wiza, "Microchannel plate detectors", Nuclear Instruments and Methods **162**, 587–601 (1979).

[49] Photonis Inc., *Long-Life™ MCP Selection Guide*, https://www.photonis.com/uploads/literature/mcp/MCP-Selection-Guide.pdf (visited on 05/11/2017).

[50] Materion CORPORATION, *AlBeMet ® Technical Fact Sheet*, https://materion.com/$%5Csim$/media/Files/PDFs/Beryllium/AlBeMet%20Materials/MAAB-032AlBeMetTechnicalDataSheet.pdf (visited on 05/11/2017).

[51] W. C. Wiley and I. H. McLaren, "Time-of-flight mass spectrometer with improved resolution", Review of Scientific Instruments **26**, 1150–1157 (1955).

[52] S. Zhang et al., "Laser-induced plasma temperature", Spectrochimica Acta - Part B Atomic Spectroscopy **97**, 13–33 (2014).

[53] VAb Vakuum-Anlagenbau GmbH., *Katalog*, May 2017, http://www.vab-vakuum.com/.

[54] EDWARDS, *Stpa803cv (tms) dn160cf inlet*, May 2017, https://shop.edwardsvacuum.com/products/yt3626003/view.aspx.

[55] M. Figueiredo and M. Carmezim, "Corrosion resistant coloured chromium oxide coatings on stainless steel", Pigment and Resin Technology **27**, 243–246 (1998).

[56] UHU, *Uhu plus endfest 2-k-epoxidharzkleber*, June 2017, http://www.uhu-profishop.de/klebeberatung/uhu-plus-endfest-300.html.

[57] Thorlabs, *Thorlabs powermeter es111c*, June 2017, https://www.thorlabs.com/thorproduct.cfm?partnumber=ES111C.

[58] CAEN, *Caen a1832 positive and negative hv board*, June 2017, http://www.caen.it/csite/CaenProd.jsp?parent=20&idmod=171.

[59] W. R. Shields et al., "Natural Variations in the Abundance Ratio and the Atomic Weight of Copper", J. Geophys. Res. **70**, 479–491 (1965).

[60] OSI Optoelectronics, *Datasheet photodiode fci-125g-006hrl*, June 2017, http://www.osioptoelectronics.com/Libraries/Datasheets/1-25-Gbps-Silicon-Photodiodes.sflb.ashx.

[61] A. Chaudhuri et al., "Carbon-cluster mass calibration at SHIPTRAP", European Physical Journal D **45**, 47–53 (2007).

[62] PfeifferVacuum, *Vacuum technology book, volume ii* (Pfeiffer Vacuum, 2017), https://www.pfeiffer-vacuum.com/de/info-center/vacuum-technology-book/.

[63] J. R. Buck, "Cavity QED in Microsphere and Fabry-Perot Cavities", PhD Thesis **2003** (2003).

[64] Agilent, *Agilent vacion plus 500 starcell*, July 2017, http://www.idealvac.com/files/ManualsII/Agilent_VacIon_Plus_500_Pumps_Manual.pdf.

[65] M. Rosenbusch et al., "Ion bunch stacking in a Penning trap after purification in an electrostatic mirror trap", Applied Physics B: Lasers and Optics **114**, 147–155 (2014).

Acknowledgements

Zunächst ein riesiges Dankeschön an Klaus Blaum. Ich bin sehr dankbar, für die von Dir geschaffene freundliche Arbeitsatmosphäre und Dein ehrliches Interesse, dass du an der Arbeit jedes Einzelnen zeigst. Die Gespräche, Kritik und Denkanstöße nicht nur im Bezug zur Arbeit, sondern auch in vielen anderen Bereichen waren mir eine Freude. Ich bin froh, dass Du es irgendwie schaffst, auch für solche Dinge Zeit zu finden, trotz deines riesigen Arbeitspensums. Danke für die tolle Betreuung.

Ein gewaltiges Danke gebührt auch Sven Sturm, der es immer wieder schafft neue Ideen zu präsentieren und gleichzeitig einen Teil seines Wissens weiter zu geben. Ich bin immer wieder verblüfft, wie viel Du in einem kurzen Gespräch erklären und vermitteln kannst und dabei neue Sichtweisen aufdeckst und Interessen weckst. Danke, dass du dir stets Zeit nimmst, danke für all die Erklärungen und danke für die gesamte schöne Zeit.

Ein weiteres großes Dankeschön auch an Robert Wolf, der mir vor allem in der Planungsphase so viel hilfreiche Tipps und Ideen gegeben hat. Deine Simion Code-Schnipsel finden sich immer noch in vielen meiner Simulationen. Danke, dass Du mir einen Einblick in dein riesiges Wissen verschafft und einen Jumpstart in Vakuumtechnik, CAD Design und Simion gegeben hast. Ich hoffe, die Australier wissen dich zu schätzen, α-Wolf!

Auch an Alex Egl ein großes Danke für deine Hilfe, wenn es mal nicht weiter ging und für die Stunden der Hilfe am Aufbau. Danke für die lustige Zeit im Labor und die dringend benötigten Feierabend-Biere.

Danke an das gesamte ALPHATRAP Team. Martin, der mit seinen Matlab Zauberkünsten stets weiter wusste und die komplexe Theorie (für mich, nicht dich) verständlich vermitteln konnte, Andi unserem Elektronik-Ass der immer passende Erklärungen hat and Ioanna for taking the time to listen to my complaints and providing helpful comments and solutions. Danke Sandro, für die Diskussionen und den Austausch zu unseren verknüpften Themen.

Danke auch an das Pentatrap-Team, das ebenfalls immer hilfsbereit zur Seite stand, wenn es im Labor etwas dringendes zu erledigen gab. Vielen Dank auch dem gesamten Team der Werkstatt, durch die aus einer Idee eine funktionierende Ionenquelle wurde.

Meinen Eltern möchte ich für die jahrelange Unterstützung danken, die es mir überhaupt erst ermöglicht hat, mein Studium abschließen zu können. Danke, dass ihr an mich geglaubt habt.

Zum Schluss möchte ich mich bei meiner Freundin Lena Walther bedanken, die mich immer wieder motivieren konnte. Danke für die Zeit mit dir, danke für deine Unterstützung und dein Verständnis. Danke, dass Du einfach uneingeschränkt für mich da warst. Danke für deine Liebe.

Erklärung:

Ich versichere, dass ich diese Arbeit selbstständig verfasst habe und keine anderen als die angegebenen Quellen und Hilfsmittel benutzt habe.

Heidelberg, den (Datum) . . . . . .